


# Summary of the BA18 Ground-Motion Model for Fourier Amplitude Spectra for Crustal Earthquakes in California

by Jeff Bayless and Norman A. Abrahamson

**Abstract** We present a summary of the [Bayless and Abrahamson \(2018b\)](#) empirical ground-motion model (GMM) for shallow crustal earthquakes in California based on the Next Generation Attenuation-West2 database ([Ancheta et al., 2014](#)). This model is denoted as BA18. Rather than the traditional response spectrum GMM, BA18 is developed for the smoothed effective amplitude spectrum (EAS), as defined by the Pacific Earthquake Engineering Research Center ([Goulet et al., 2018](#)). The EAS is the orientation-independent horizontal-component Fourier amplitude spectrum of ground acceleration. The model is developed using a database dominated by California earthquakes but takes advantage of crustal earthquake data worldwide to constrain the magnitude scaling and geometric spreading. The near-fault saturation is guided by finite-fault numerical simulations, and nonlinear site amplification is incorporated using a modified version of [Hashash et al. \(2018\)](#). The model is applicable for rupture distances of 0–300 km,  $M$  3.0–8.0, and over the frequency range 0.1–100 Hz. The model is considered applicable for  $V_{S30}$  in the range 180–1500 m/s, although it is not well constrained for  $V_{S30}$  values  $>1000$  m/s. Models for the median and the aleatory variability of the EAS are developed. Regional models for Japan and Taiwan will be developed in a future update of the model. A MATLAB program that implements the EAS GMM is provided in the  supplemental content to this article.

*Supplemental Content:* MATLAB program that implements the BA18 ground-motion model. The function includes all model coefficients required to predict the median effective amplitude spectrum (EAS) and associated standard deviations over the frequency range 0.1–100 Hz.

## Introduction

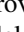
Ground-motion models (GMMs) are used for estimating the level of ground shaking at a site, including the variability in that level, based on earthquake magnitude, source-to-site distance, local site conditions, and other seismological parameters. Among other applications, GMMs are often used in deterministic or probabilistic seismic hazard analyses to develop design ground motions. GMMs can be developed using recorded ground motions, using numerical earthquake simulations, or a combination of both approaches. The traditional approach for developing GMMs for engineering applications is to use response spectral values (typically 5% damped pseudospectral acceleration [PSA]) for a range of spectral periods. The response spectral values represent the response of a simple structure to the input ground motion, which is influenced by a range of Fourier frequencies and does not directly represent the ground motion itself. As an alternative, Fourier amplitude spectral (FAS) values can be used instead of response spectral values. There are several advantages using FAS in place of response spectra when

developing a GMM: (1) the scaling of FAS in the GMM is easier to constrain using seismological theory, and numerous seismological models of the FAS are available (e.g., [Brune, 1970](#); [Boore et al., 2014](#)) to provide a frame of reference during model development; (2) linear site response remains linear at all frequencies and does not depend on the spectral content of the input motion, as is the case for response spectra ([Bora et al., 2016](#)); and (3) for calibrating input parameters and methods for finite-fault simulations based on comparisons with GMMs, Fourier spectra are more closely related to the physics in the simulations.

In forward application, an FAS GMM can be used as a stand-alone replacement for a response spectrum GMM in seismic hazard assessments, or the FAS and duration models can be combined within the random vibration theory (RVT) framework to obtain the response spectrum (e.g., [Bora et al., 2019](#)). In addition, the residuals from a FAS model can be used to develop models for the inter-frequency correlation of FAS, and correlation models based on FAS can facilitate

future calibration of methods for simulating the ground motions generated by earthquakes (e.g., Bayless and Abrahamson, 2018a,c), can be used to generate conditional mean spectra for FAS, or can be used to conduct vector-valued probabilistic seismic hazard analyses for FAS (Abrahamson, 2006).

In this article, an empirical Fourier spectrum GMM for shallow crustal earthquakes in California based on the Pacific Earthquake Engineering Research Center (PEER) Next Generation Attenuation-West2 (NGA-West2) database (Ancheta *et al.*, 2014) is developed. The ground-motion parameter used in the GMM is the smoothed EAS, as defined by PEER (Goulet *et al.*, 2018). The EAS is the orientation-independent horizontal-component FAS of ground acceleration that can be used with RVT to estimate the response spectral values.

In this article, we summarize the BA18 model, including the selection of the ground-motion data, the basis for the functional form of the model, a description of the Maechling *et al.* (2015) finite-fault simulations used to constrain the near-fault large-magnitude scaling, and an explanation of the analytical site response modeling to capture the nonlinear site amplification (Hashash *et al.*, 2018). Bayless and Abrahamson (2018b) give a complete description of the model behavior and a comprehensive set of residual plots. Rather than simply fitting the empirical data, emphasis is placed on building the model using both the empirical data and analytical results from these seismological and geotechnical models so that the GMM extrapolates in a reasonable manner. A MATLAB program (see Data and Resources) that implements the EAS GMM is provided in the  supplemental content to this article. A model for the interfrequency correlation of residuals derived from this GMM is presented by Bayless and Abrahamson (2018c).

#### EAS Ground-Motion Intensity Measure

EAS is defined Goulet *et al.* (2018) and is calculated for an orthogonal pair of FAS using the following equation:

$$\text{EAS}(f) = \sqrt{\frac{1}{2}[\text{FAS}_{\text{HC1}}(f)^2 + \text{FAS}_{\text{HC2}}(f)^2]}, \quad (1)$$

in which  $\text{FAS}_{\text{HC1}}$  and  $\text{FAS}_{\text{HC2}}$  are the FAS of the two as-recorded orthogonal horizontal components of the ground motion and  $f$  is the frequency in hertz, and the FAS are processed by PEER following the procedure given by Kishida *et al.* (2016). The EAS is independent of the orientation of the instrument. Using the average power of the two horizontal components leads to an amplitude spectrum that is compatible with the use of RVT to convert Fourier spectra to response spectra. The EAS is smoothed using the  $\log_{10}$ -scale Konno and Ohmachi (1998) smoothing window, which has weights and window parameter defined as follows:

$$W(f) = \left( \frac{\sin(b \log(f/f_c))}{b \log(f/f_c)} \right)^4, \quad (2)$$

$$b = 2\pi/b_w. \quad (3)$$

The smoothing parameters ( $W, f_c, b, b_w$ ) are described by Kottke *et al.* (2018, p. 38):

*W* is the weight defined at frequency  $f$  for a window centered at frequency  $f_c$  and defined by the window parameter  $b$ . The window parameter  $b$  can be defined in terms of the bandwidth, in  $\log_{10}$  units, of the smoothing window,  $b_w$ .

The Konno and Ohmachi smoothing window was selected by PEER NGA-East (Pacific Earthquake Engineering Research Center [PEER], 2015) because it led to minimal bias on the amplitudes of the smoothed EAS compared with the unsmoothed EAS. The bandwidth of the smoothing window  $b_w = 0.0333$  was selected such that four RVT calibration properties (the zeroth spectral moment, delta [measure of ground-motion bandwidth], the frequency of zero crossings, and the frequency of extrema) before and after smoothing were minimally affected (Kottke *et al.*, 2018). Using the smoothed EAS with the same smoothing bandwidth maintains consistency with the PEER database and with other PEER projects, including the NGA-East empirical FAS models (Goulet *et al.*, 2018). This allows direct comparison of the median and standard deviation of the GMMs based on the PEER data sets.

#### Ground-Motion Data

The PEER NGA-West2 strong-motion database, described by Ancheta *et al.* (2014), includes >21,000 three-component strong-motion records recorded worldwide from shallow crustal earthquakes, including aftershocks, in active tectonic regimes. Earthquake magnitudes in the full database range from 3 to 7.9, and rupture distances extend to over 1500 km. Earthquakes and recordings identified as questionable in quality or with undesirable properties are excluded; see Abrahamson *et al.* (2014) for a complete list of criteria for exclusions. At distances under 100 km, recordings from crustal earthquakes worldwide are retained to constrain the magnitude scaling and geometric spreading. At the larger distances ( $\leq 300$  km), region-specific anelastic attenuation and linear site effects due to the regional crustal structure are accounted for by including recordings only from California and western Nevada. Only events with at least five recordings per earthquake are included.

The FAS has been calculated for each record in the database up to the Nyquist frequency by PEER (Kishida *et al.*, 2016). The usable frequency range limitations of each record are accounted for by applying the recommended lowest and

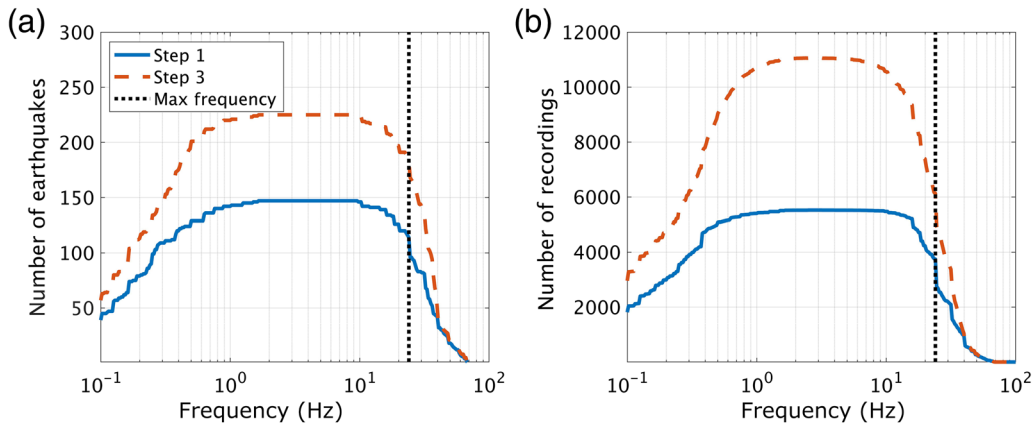


**Figure 1.** Number of earthquakes and recordings from the Next Generation Attenuation-West2 (NGA-West2) effective amplitude spectrum (EAS) database used in the regression steps (a) 1 and (b) 3 versus frequency. The regressions were performed between 0.1 and 24 Hz, and higher frequencies are shown to display the rapid reduction of available data with increasing frequency. The color version of this figure is available only in the electronic edition.

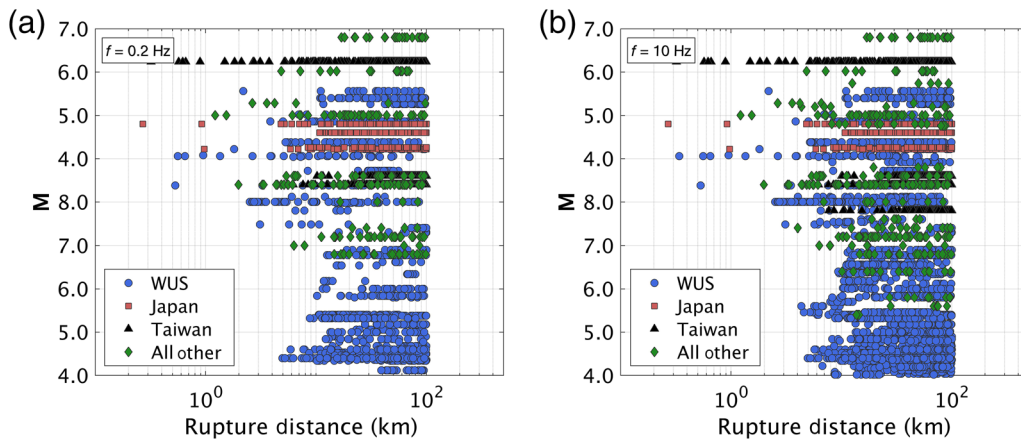


**Figure 2.** Magnitude versus rupture distance pairs of the NGA-West2 EAS database subset used in regression step 1, at (a) 0.2 and (b) 10.0 Hz. The color version of this figure is available only in the electronic edition.

highest usable frequencies for response spectra determined from Abrahamson and Silva (1997) as

$$\begin{aligned} \text{Lowest usable frequency (LUF)} \\ = 1.25 \times \max(\text{HPF}_{\text{HC1}}, \text{HPF}_{\text{HC2}}), \end{aligned} \quad (4)$$

$$\begin{aligned} \text{Highest usable frequency (HUF)} \\ = \frac{1}{1.25} \times \min(\text{LPF}_{\text{HC1}}, \text{LPF}_{\text{HC2}}), \end{aligned} \quad (5)$$

in which HPF is the record high-pass filter frequency, LPF is the record low-pass filter frequency, and HC1 and HC2 are the two horizontal components of a three-component time series. The factors of 1.25 in equations (4) and (5) were originally used by Abrahamson and Silva (1997) to ensure that the filters did not have a significant effect on the response spectral values. By limiting the usable period range using these factors, the frequency interval of the impulse response of a 5%

damped oscillator will not exceed the filter values. And retaining this usable frequency range maintains consistency with the response spectrum calculations. Based on inspection of the usable frequency range of the data shown in Figure 1, the regressions were performed between 0.1 and 24 Hz.

After screening for record quality, recording distance, minimum station requirements, and frequency limitations, the final dataset consists of 13,346 unique records from 232 earthquakes, both of which vary as a function of frequency. Figure 1 shows the frequency dependence of the number of earthquakes and recordings used in regression steps 1 and 3 (as explained subsequently). Figure 2 shows a magnitude versus rupture distance scatterplot of the NGA-West2 database subsets used in regression step 1 at  $f = 0.2$  and 10 Hz.

### Median Model Functional Form

The model parameters are defined in Table 1. The scaling of the source is primarily described by moment

**Table 1**  
Model Parameter Definitions

| Parameter        | Definition   |
|------------------|--|
| EAS              | Effective amplitude spectrum ( $g \cdot s$ ). The EAS is the orientation-independent horizontal-component Fourier amplitude spectrum (FAS) of ground acceleration, defined in <a href="#">Goulet et al. (2018)</a> . |
| $M$              | Moment magnitude   |
| $Z_{\text{tor}}$ | Depth from the surface to the top of the rupture plane (kilometers)  |
| $F_{\text{NM}}$  | Style-of-faulting flag: 1 for normal-faulting earthquakes; 0 for all others  |
| $R_{\text{rup}}$ | Rupture distance (kilometers)  |
| $V_{S30}$        | Time averaged shear-wave velocity in the upper 30 m (m/s)  |
| $Z_1$            | Depth from the surface to shear-wave velocity horizon of at least 1 km/s (km)  |
| $I_r$            | Peak ground acceleration for the $V_{S30} = 760$ m/s condition ( $g$ )   |

magnitude ( $M$ ). Source effects are also modeled using the depth to the top of the rupture plane ( $Z_{\text{tor}}$ ) and a style-of-faulting flag for normal faults ( $F_{\text{NML}}$ ). These source effects can be considered as proxies for stress-drop scaling. The closest distance to the rupture plane  $R_{\text{rup}}$  is used as the distance measure for path scaling. The linear and nonlinear site effects are parameterized using  $V_{S30}$ , the time-averaged shear-wave velocity in the top 30 m of the soil column below the site. Use of  $V_{S30}$  does not imply that 30 m is the key depth range for the site response but rather that  $V_{S30}$  is correlated with the deeper soil profile ([Abrahamson and Silva, 2008](#)). The scaling with respect to soil depth is parameterized by the depth to shear-wave velocity of 1 km/s,  $Z_1$ .

The model for the EAS (units  $g$ -second [ $g \cdot s$ ]) ground motion is given by the following equation

$$\ln \text{EAS} = \ln \text{EAS}_{\text{med}} + \epsilon\sigma, \quad (6)$$

in which  $\sigma$  is the total aleatory variability and the standard normal random variable  $\epsilon$  is the number of logarithmic standard deviations above or below the median. The model for the median EAS ( $\text{EAS}_{\text{med}}$ , with units  $g \cdot s$ ) is formulated as

$$\ln \text{EAS}_{\text{med}} = f_M + f_P + f_S + f_{Z_{\text{tor}}} + f_{\text{NM}} + f_{Z_1}, \quad (7)$$

in which each of the model components in equation (7) is described in the following sections.

#### Magnitude Scaling $f_M$

To capture the effects of energy radiated at the source, the formulation of the magnitude scaling is adopted from the [Chiou and Youngs \(2014, 2008\)](#) GMMs for response spectra. A polynomial magnitude scaling formulation was tested (e.g., [Abrahamson et al., 2014](#)) and after evaluating the data found that both formulations fit the data well, but the [Chiou and Youngs \(2008, 2014\)](#) formulation would extrapolate more reasonably. In addition, the [Chiou and Youngs](#)

(2008, 2014) formulation has undergone several years of testing and refinement and is based on seismological models for the source FAS, which translates directly to this application. The expression for the magnitude scaling is given by

$$f_M = c_1 + c_2(M - 6) + \frac{(c_2 - c_3)}{c_n} \ln(1 + e^{c_n(c_M - M)}). \quad (8)$$

The components of  $f_M$  are described in [Chiou and Youngs \(2008\)](#). To recap, the formulation captures approximately linear magnitude scaling at low frequencies (well below the source corner) and high frequencies (well above the source corner) with a nonlinear transition in between, in which the transition shifts to larger magnitude for lower frequencies. The  $c_1$  term works jointly with the  $c_2$  and  $c_3$  terms to represent the median spectral shape after correcting for all other adjustments. The coefficient  $c_2$  is the frequency-independent linear  $M$  scaling slope for frequencies well above the theoretical corner frequency. The  $(c_2 - c_3)/c_n$  term captures both the linear scaling of the FAS below the theoretical corner frequency (coefficient  $c_3$ ) and the nonlinear transition to that scaling. The coefficient  $c_n$  controls the width of the magnitude range over which the transition between low- and high-frequency linear scaling occurs; the coefficient  $c_M$  is the magnitude at the midpoint of this transition. All of the magnitude scaling terms were determined in the regression.

#### Path Scaling $f_P$

Together with the magnitude scaling, the path scaling formulation of [Chiou and Youngs \(2014\)](#) is used:

$$f_P = c_4 \ln(R_{\text{rup}} + c_5 \cosh(c_6 \max(M - c_{hm}, 0))) + (-0.5 - c_4) \ln(\hat{R}) + c_7 R_{\text{rup}}, \quad (9)$$

in which  $\hat{R} = \sqrt{R_{\text{rup}}^2 + 50^2}$ . The components of equation (9) are described by [Chiou and Youngs \(2008\)](#). To recap, the  $c_4$  term captures the near-source geometric spreading, which is magnitude and frequency dependent. The magnitude and frequency dependence on the geometric spreading is introduced by adding a term to the rupture distance inside the log-distance term, expressed by the  $c_5$  term. This additive distance is designed to capture the near-source amplitude saturation effects of the finite-fault rupture dimension. This term is a frequency-dependent constant for small magnitudes and transitions to be proportional to  $\exp(M)$  for large magnitudes, with the largest additive distance at high frequencies. Because the hyperbolic cosine is a monotonically increasing function, the coefficient  $c_5$  controls the scaling of this term, and coefficients  $c_6$  and  $c_{hm}$  control the gradient.

Because the coefficients  $c_5$ ,  $c_6$ , and  $c_{hm}$  are multiplied by  $c_4$ , there is potential for trade-off between them. The regression procedure is started with the values for coefficients  $c_5$ ,  $c_6$ , and  $c_{hm}$  from [Chiou and Youngs \(2014\)](#) to obtain  $c_4$  from the data, ensuring the model did not oversaturate. Using equations (8) and (9), the full saturation



condition (no magnitude scaling at zero distance) leads to the following constraint on the coefficients:  $c_2 = -c_4c_6$ . For  $c_2$  values larger than the full saturation value, there will be a positive magnitude scaling at zero distance (i.e., not full saturation). It is reasonable for the EAS to have some scaling at zero distance even though the PSA is nearly fully saturated at high frequencies. The PSA saturates, in part, because the PSA is defined by the peak response of the oscillator over all time, meaning it is not affected by longer duration of the signal with lower amplitudes that do not contribute to the peak response. Conversely, the EAS is not a peak response operator, so it will continue to scale for large magnitudes at short distance because of the longer source durations. This is the contribution of the lower amplitudes over the duration of the signal.

The near-source saturation of magnitude scaling is checked against the data and against finite-fault simulations (see the [Model Summary](#) section for more details). The EAS saturation in this model agrees with those from the simulations. In later stages of the regression, the coefficients  $c_5$ ,  $c_6$ , and  $c_{hm}$  are also determined empirically. The values from the regression did not change enough to impact the model, so coefficient values are fixed from [Chiou and Youngs \(2014\)](#) for  $c_5$ ,  $c_6$ , and  $c_{hm}$  in the final model. Thus, the coefficients  $c_2$  and  $c_4$  control the saturation in the model development.

Following [Chiou and Youngs \(2014\)](#), at large distances, the distance scaling smoothly transitions to be proportional to  $R^{-0.5}$  to model surface wave rather than body-wave geometric spreading effects. This effect is introduced with  $\ln(\hat{R})$  term, which controls at distances greater than 50 km by subtracting the  $c_4$  coefficient and imposing a  $-0.5$  slope. Both values of  $-0.5$  slope and 50 km break distance were adopted from [Chiou and Youngs \(2014\)](#) and did not introduce any bias in residuals; therefore, these values were fixed. Effects of crustal anelastic attenuation (Q) are captured through the frequency-dependent coefficient  $c_7$  term. The Q scaling does not require magnitude dependence for the EAS.

#### Site Response $f_S$

The  $V_{S30}$  (m/s) dependence of site amplification is modeled using the form:

$$f_S = f_{SL} + f_{NL}, \quad (10a)$$

$$f_{SL} = c_8 \ln\left(\frac{\min(V_{S30}, 1000)}{1000}\right), \quad (10b)$$

$$f_{NL} = f_2 \ln\left(\frac{I_R + f_3}{f_3}\right), \quad (10c)$$

$$f_2 = f_4(e^{f_5(\min(V_{S30}, V_{ref})-360)} - e^{f_5(V_{ref}-360)}), \quad (10d)$$

$$\ln(I_R) = 1.238 + 0.846 \ln(\text{EAS}_{ref}(f = 5 \text{ Hz})). \quad (10e)$$

in which the linear site amplification is given by  $f_{SL}$ , and the nonlinear site amplification is given by  $f_{NL}$ , which is the analytical site amplification function for FAS in the western United States (WUS) modified from [Hashash et al. \(2018\)](#).

The linear site term,  $f_{SL}$ , is formulated as a linear function of  $\ln(V_{S30})$  and is centered on the reference value of  $V_{S30} = 1000$  m/s. The  $f_{SL}$  term coefficients are determined in the regression analysis. [Abrahamson et al. \(2014\)](#) observed that the scaling of PSA with  $V_{S30}$  became weaker for higher  $V_{S30}$  values. Therefore, we selected a model that does not scale with  $V_{S30}$  above some maximum value  $V_1 = 1000$  m/s. The weak  $V_{S30}$  scaling at high  $V_{S30}$  values implies that the correlation between  $V_{S30}$  and the deeper part of the  $V_s$  profile that controls site amplification is much weaker for hard-rock site than for soil sites. Below 1000 m/s, the linear site amplification terms approximately scales linearly with  $\ln(V_{S30})$ , so the regional linear  $V_{S30}$ -based site amplification is modeled with a single frequency-dependent coefficient  $c_8$ .

The nonlinear site amplification,  $f_{NL}$ , is constrained using a purely analytical model rather than obtaining it from the data. Empirical evaluations of the nonlinear effects are limited by the relatively sparse sampling of ground motions expected to be in the nonlinear range in the NGA-West2 database ([Kamai et al., 2014](#)). Therefore, the [Hashash et al. \(2018\)](#) nonlinear site amplification term,  $f_{NL}$ , is adopted to model nonlinear soil amplification. In [Hashash et al. \(2018\)](#), the site response analysis software DEEPSOIL version 6.1 (V6.1) ([Hashash et al., 2016](#)) is used to perform a large number of 1D site response simulations (30,000+) of input rock motions propagated through soil columns representative of WUS site conditions. The [Hashash et al. \(2018\)](#) nonlinear analyses are conducted in the time domain using the implicit integration of the equation of motion. The soil properties in these simulations represent a range of geologic conditions in the western United States modeled as 1D profiles, with specific  $V_s$  profiles and properties from [Kim et al. \(2016\)](#), and seed  $V_s$  profiles for randomization from [Walling et al. \(2008\)](#). [Hashash et al. \(2018\)](#) produced linear and nonlinear analytical site amplification models for the PSA and FAS; only the nonlinear FAS model is adopted here.

Equations (10c) and (10d) are the nonlinear FAS amplification components of the [Hashash et al. \(2018\)](#) model developed for the WUS. In these equations,  $f_3$ ,  $f_4$ , and  $f_5$  are frequency-dependent coefficients;  $I_R$  is the peak ground acceleration (PGA, in units  $g$ ) at rock outcrop; and  $V_{ref} = 760$  m/s is the limiting  $V_{S30}$  condition beyond which there is no nonlinear amplification ([Hashash et al., 2018](#)). In this model, almost no nonlinearity is applied at frequencies below 1.0 Hz and the modification approaches zero for small values of the input motion ( $I_R$ ) and as  $V_{S30}$  approaches  $V_{ref}$ .

To ensure smooth spectra in the GMM, a smoothed version of the [Hashash et al. \(2018\)](#) nonlinear site amplification model is implemented. The smoothing of coefficients  $f_3$ ,  $f_4$ , and  $f_5$  is performed in log-frequency space. The maximum frequency of the [Hashash et al. \(2018\)](#) model

is 13.3 Hz, and the coefficients of the model reduce the nonlinear effect to zero for frequencies greater than this value simply because of the lack of FAS values at higher frequencies. Physically, this is not realistic behavior. To include nonlinear effects at the higher frequencies, the Hashash *et al.* (2018) model is modified by taking the following procedure for a given scenario ( $\mathbf{M}$ ,  $R_{rup}$ ,  $V_{S30}$ , etc): calculate  $f_{NL}$  over all frequencies (0.1–100 Hz), take the minimum value of  $f_{NL}$  over these frequencies ( $f_{NL,min}$ ), and constrain all frequencies higher than the frequency corresponding to  $f_{NL,min}$  to take the value of  $f_{NL,min}$ . That is, the maximum nonlinear effect for a given scenario is assumed to apply to the high frequencies. An example of this procedure is illustrated in figure 3.2 of Bayless and Abrahamson (2018b).

The Hashash *et al.* (2018) nonlinear site amplification model requires the PGA on rock. Because the model described here is for the EAS, an estimate of the PGA (in units  $g$ ) for the reference site condition is developed as a function of the EAS for the reference site condition at  $f = 5$  Hz (in units  $g \cdot s$ ), given by equation (10e). The EAS at  $f = 5$  Hz is used to estimate PGA because this is approximately the predominant frequency of the ground motions (response spectra generally peak at  $T = 0.2$  s) and should correlate strongly with the PGA. To develop the  $I_R - EAS_{ref}(f = 5 \text{ Hz})$  relationship, a subset of the ground motions from the  $f = 24$  Hz regression having as-recorded  $I_R > 0.01g$  are corrected to the reference site condition using the Abrahamson *et al.* (2014) linear site amplification model, and the EAS is corrected to the reference  $V_{S30}$  condition using the linear site amplification model from this study. From this database, the relationship given by equation (10e) is developed (Bayless and Abrahamson, 2018b; their fig. 3.3). The slope of equation (10e) is not strongly dependent on the different  $\mathbf{M}$  and distance ranges evaluated.

#### Depth to Top of Rupture Scaling $f_{Z_{tor}}$

To model differences in the ground motions for surface and buried ruptures, the depth-to-top-of-rupture scaling model takes the form

$$f_{Z_{tor}} = c_9 \min(Z_{tor}, 20), \quad (11)$$

in which  $c_9$  is the frequency dependent and  $Z_{tor}$  is the depth to the top of rupture, measured in kilometers. The  $Z_{tor}$  scaling is capped at 20 km, selected based on the data used to develop the model, to prevent unbounded scaling with  $Z_{tor}$ .

#### Normal Style-of-Faulting Effects $f_{NM}$

To model the differences in ground motions for normal style of faulting, the normal-faulting term is

$$f_{NM} = c_{10} F_{NM}, \quad (12)$$

in which  $F_{NM}$  is 1 for normal faults and 0 for all others and  $c_{10}$  is determined in the regression. A normal fault is defined

by rake angle between  $-150^\circ$  and  $-30^\circ$ . A style-of-faulting term for reverse events was considered (in which a reverse event is defined by rake angle between  $30^\circ$  and  $150^\circ$ ) but not included because this term was highly correlated with  $Z_{tor}$ . Therefore, the reverse style-of-faulting scaling is captured in the  $f_{Z_{tor}}$  scaling.

#### Soil Depth Scaling $f_{Z1}$

To model the scaling with respect to sediment thickness, the Abrahamson *et al.* (2014) formulation is adopted, which is parameterized by the depth to the shear-wave velocity horizon of 1.0 km/s,  $Z_1$  (units of kilometers). This model takes the form

$$f_{Z1} = c_{11} \ln\left(\frac{\min(Z_1, 2.0) + 0.01}{Z_{1Ref} + 0.01}\right), \quad (13a)$$

$$c_{11} = \begin{cases} c_{11a} & \text{for } V_{S30} \leq 200 \text{ m/s} \\ c_{11b} & \text{for } 200 < V_{S30} \leq 300 \text{ m/s} \\ c_{11c} & \text{for } 300 < V_{S30} \leq 500 \text{ m/s} \\ c_{11d} & \text{for } V_{S30} > 500 \text{ m/s} \end{cases}, \quad (13b)$$

$$Z_{1Ref} = \frac{1}{1000} \exp\left(\frac{-7.67}{4} \ln\left(\frac{V_{S30}^4 + 610^4}{1360^4 + 610^4}\right)\right), \quad (13c)$$

in which  $Z_{1Ref}$  is the reference  $Z_1$  based on  $V_{S30}$  for the regional model for California (Abrahamson *et al.*, 2014; their equation 18). Equation (13c) was developed by Chiou and Youngs (2014) to account for the  $V_{S30} - Z_1$  relationships in the data. Abrahamson *et al.* (2014) showed that the  $Z_1$  scaling is correlated with the  $V_{S30}$  values, and they used the  $V_{S30}$  bins in Equation (13b) to model this dependence. The soil-depth scaling of the proposed model (equation 13a) is capped to  $Z_1 = 2$  km based on the range of the data used in the model and to avoid unconstrained extrapolation. The value  $Z_1 = 2$  km was selected because 99% of the recordings used in the regression have  $Z_1$  values  $< 2$  km.

#### Regression Analysis

The random-effects model is used for the regression analysis following the procedure described by Abrahamson and Youngs (1992). This procedure leads to the separation of total residuals into between-event residuals ( $\delta B$ ) and within-event residuals ( $\delta W$ ) following the notation of Al Atik *et al.* (2010). For large number of recordings per earthquake, the between-event residual is approximately the average difference in logarithmic space between the observed intensity measure (IM) from a specific earthquake and the IM predicted by the GMM. The within-event residual ( $\delta W$ ) is the difference between the IM at a specific site for a given earthquake and the median IM predicted by the GMM plus

**Table 2**  
Regression Steps

| Step | Data Used  | Parameters Free in the Regression                             | Parameters Smoothed after the Regression |
|------|--|---|--|
| 1a   | $M > 4$ , $R_{rup} \leq 100$ km, all regions                   | $c_1, c_2, c_3, c_n, c_M, c_4, c_7, c_8, c_9, c_{10}, c_{11}$ | $c_2, c_4$ ( $\mathbf{M}$ , path)        |
| 1b   | Same as 1a   | $c_1, c_3, c_n, c_M, c_7, c_8, c_9, c_{10}, c_{11}$           | $c_3, c_n, c_M$ ( $\mathbf{M}$ )         |
| 1c   | Same as 1a   | $c_1, c_5, c_6, c_{hm}, c_7, c_8, c_9, c_{10}, c_{11}$        | $c_5, c_6, c_{hm}$ (path)                |
| 1d   | Same as 1a   | $c_1, c_7, c_8, c_9, c_{10}, c_{11}$                          | $c_9$ ( $Z_{tor}$ )                      |
| 1e   | Same as 1a   | $c_1, c_7, c_8, c_{10}, c_{11}$                               | $c_{10}$ ( $F_{NM}$ )                    |
| 2    | $M > 4$ , $R_{rup} \leq 100$ km from California/western Nevada | $c_1, c_7, c_8, c_{11}$                                       | $c_8$ ( $V_{S30}$ )                      |
| 3a   | $M > 3$ , $R_{rup} \leq 300$ km from California/western Nevada | $c_1, c_7, c_{11}$  | $c_{11}$ ( $Z_1$ )                       |
| 3b   | Same as 3a   | $c_1, c_7$  | $c_7$ ( $Q$ )                            |
| 3c   | Same as 3a   | $c_1$   | $c_1$                                    |

$\delta B$ . By accounting for repeatable site effects,  $\delta W$  can further be partitioned into a site-to-site residual ( $\delta S_2S$ ) and the single-station within-event residual ( $\delta WS$ , also called the within-site residual) using a mixed-effects regression on the  $\delta W$  with random effects for the site-to-site terms (e.g., Villani and Abrahamson, 2015). Using this notation, the residuals take the following form:

$$Y = g(X_{es}, \theta) + \delta B_e + \delta S_2S_s + \delta WS_{es}, \quad (14)$$

$$\delta_{total} = Y - g(X_{es}, \theta) = \delta B_e + \delta S_2S_s + \delta WS_{es}, \quad (15)$$

in which  $Y$  is the natural log of the recorded ground-motion IM,  $g(X_{es}, \theta)$  is the median GMM,  $X_{es}$  is the vector of explanatory seismological parameters (magnitude, distance, site conditions, etc.),  $\theta$  is the vector of GMM coefficients, and  $\delta_{total}$  is the total residual for earthquake  $e$  and site  $s$ .

The residual components  $\delta B$ ,  $\delta S_2S$ , and  $\delta WS$  are well represented as zero mean, independent, normally distributed random variables with standard deviations  $\tau$ ,  $\phi_{S_2S}$ , and  $\phi_{SS}$ , respectively (Al Atik *et al.*, 2010). The total standard deviation  $\sigma$  is expressed as

$$\sigma = \sqrt{\tau^2 + \phi_{S_2S}^2 + \phi_{SS}^2}. \quad (16)$$

The regression is performed in a series of steps to prevent trade-off of correlated model coefficients and to constrain different components of the model using the data relevant to each piece. These steps are given in Table 2 along with the data used and parameters determined from each step. In step 1a, a data set consisting of larger magnitudes and shorter distances from all regions is used to constrain the magnitude scaling in the large magnitude range and the near-source finite-fault saturation. In steps 1b–d, the same data set is used, and the remaining source effects are determined. In step 2, the regionalized linear site amplification parameters are determined using the data from California and western Nevada at distances within 100 km. In steps 3a–c, data from California and western Nevada are included out to 300 km distance. In these regression steps, the regional soil depth

scaling, anelastic attenuation, and mean spectral shape coefficients are determined. For all steps, the regression is performed independently at each of 239 log-spaced frequencies spanning 0.1–24 Hz.

### Smoothing

The model coefficients are smoothed in a series of steps as outlined in Table 2. Smoothing of the coefficients is performed to assure smooth spectra and, in some cases, to constrain the model to a more physical behavior in which the data are sparse (Abrahamson *et al.*, 2014). Tables of the values of the final smoothed coefficients are available in the [E](#) supplemental content to this article.

Figure 3 shows the regressed model coefficients plotted versus frequency before and after smoothing. The smoothed coefficients  $c_2$  and  $c_4$  are frequency independent and are determined from regressions in the high-frequency range. The coefficients  $c_3$ ,  $c_n$ , and  $c_M$  require only minor smoothing to assure smooth spectra in the final model, including extrapolation outside the ranges well constrained by data. The smoothing of  $c_7$  (the anelastic attenuation term) is constrained to be nonpositive at all frequencies so that the model does not unintentionally increase in amplitude at very large distances. Minimal smoothing is required for the coefficient  $c_8$  (the linear  $V_{S30}$  term). The coefficient  $c_9$  (the  $Z_{tor}$  term) takes on negative values at low frequencies, implying small deamplification of low-frequency ground motions with increasing  $Z_{tor}$ . The data lead to a large drop in  $c_{10}$  (the normal-faulting term) at low frequencies, but this is not included in the model because the theoretical basis is not clear; instead a frequency-independent constant is used (uniform scaling across frequencies) for normal style-of-faulting earthquakes. The  $c_{11}$  terms are smoothed as shown in Figure 3, in which the uncertainty is largest for  $c_{11a}$ , which corresponds to the lowest  $V_{S30}$  bin with relatively fewer data.

The  $c_1$  coefficient works collectively with the  $c_3$  term to represent the mean spectral shape after correcting for all other adjustments. In the regression, unexpected behavior of  $c_1$  at low frequencies is observed. At frequencies below  $\sim 0.3$  Hz, the regressed coefficient values are equal to or larger than the 0.3 Hz value. If unmodified and combined with the  $c_3$  term, this would lead to an irregular spectral

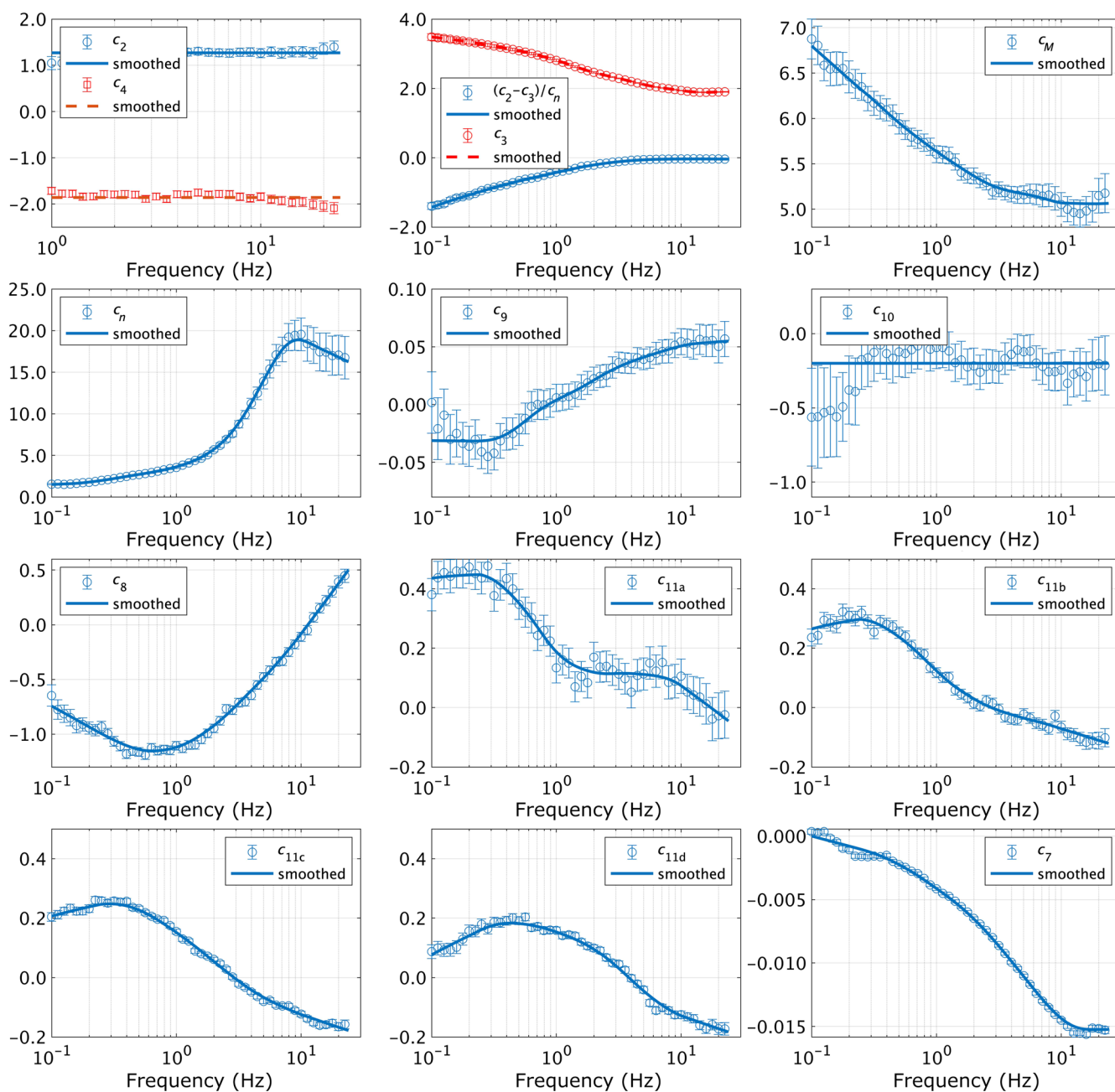


**Figure 3.** Smoothing of the model coefficients. The color version of this figure is available only in the electronic edition.

bump at  $f < 0.3$  Hz. Following [Aki \(1967\)](#), the mean spectrum should be approximately linear with a two-slope in this frequency range. Therefore, the  $c_1$  coefficient is modified at low frequencies by constraining the slope from  $f \approx 1.0$  Hz down to 0.1 Hz. The difference between the regressed values of  $c_1$  and the constrained values of  $c_1$  is denoted  $c_{1a}$ . By introducing the  $c_{1a}$  term, the model predicts smooth, theoretically appropriate spectra at low frequencies. This also allows for residuals that are zero centered, which is required for computing the correlations of the residuals between frequencies. To account for this modification, the  $c_{1a}$  term must be added to the total standard deviation using

equation (18). The standard deviation model is discussed further subsequently.

This unexpected behavior of  $c_1$  may be due to bias in the data. At low frequencies, the signal-to-noise ratio is commonly low ([Douglas and Boore, 2011](#)). This contributes to the drop off in data at low frequencies shown in [Figure 1](#). In addition, at low frequencies, the large epsilon (above average) ground motions are more likely to be above the signal-to-noise ratio and therefore to be included in the database. Similarly, the below-average ground motions are more likely to be below this ratio and be excluded. The net effect may be that for the FAS at low frequencies, the database is biased



toward higher ground motions. [Chiou and Youngs \(2008\)](#) also noted similar irregular steps in their  $c_1$  at spectral periods with large reductions in the number of usable data and suggested that these coefficient estimates may be biased toward larger ground-motion amplitude data.

Other physical explanations of the cause of the increase in coefficient  $c_1$  are not apparent. To check that long-period basin effects are not the cause, the mean spectra are examined in the same way but only including records with  $Z_1 < 0.15$  km, and the same behavior is observed. To further test if basin effects are not adequately captured by the model,  $c_1$  is fixed to the constrained shape, and the spatial distribution of the residuals is plotted on maps. These maps of residuals did not have consistent regional or spatial trends, implying that basin effects are not the culprit. Understanding the physical cause of the long-period shape of the spectrum will be evaluated further in a future study.

#### Extrapolation to 100 Hz

Model coefficients are obtained by regression for frequencies up to 24 Hz. At high frequencies, the FAS decays rapidly ([Hanks, 1982](#); [Anderson and Hough, 1984](#)). [Anderson and Hough \(1984\)](#) introduced the spectral decay factor kappa ( $\kappa$ ) to model the rate of the decrease, in which the amplitude of the log(FAS) decays linearly versus frequency (linear spaced), and  $\kappa$  is related to the slope. The total site amplification is the combined effect of crustal amplification and damping ( $\kappa$  and  $Q$ ), but the effect of  $\kappa$  is so strong that it controls the spectral decay of the FAS at high frequencies and is the only parameter specified in the extrapolation. The model is extrapolated using the following equations:

$$D(\kappa, f) = \exp(-\pi\kappa f), \quad (17a)$$

$$\ln(\kappa) = -0.4 \times \ln\left(\frac{V_{S30}}{760}\right) - 3.5, \quad (17b)$$

$$\text{EAS}(f > 24 \text{ Hz}) = \text{EAS}(f = 24 \text{ Hz}) \times D(\kappa, f - 24), \quad (17c)$$

in which  $D(\kappa, f)$  is the [Anderson and Hough \(1984\)](#) diminution operator and 24 Hz is the frequency beyond which the extrapolation occurs. The parameter  $\kappa$  is estimated from  $V_{S30}$  using the relationship given by equation (17b). This relationship is selected based on the range of  $\kappa_0 - V_{S30}$  correlation models presented in figure 2 of [Ktenidou et al. \(2014\)](#). The scatter observed in these correlations is large, as described by [Ktenidou et al. \(2014\)](#).

#### Residuals

The model is evaluated by checking the residuals from the regression analysis as functions of the main model parameters. Example residual plots are included here; a

larger set of residual plots are available in [Bayless and Abrahamson \(2018b\)](#); their appendix A).

#### Between-Event and Between-Site Residuals

The dependence on the source parameters of the between-event residuals at  $f = 5.0$  Hz is given in Figure 4. In this figure, the diamond-shaped markers represent events from California and western Nevada, and circles represent events from all other regions; at distances under 100 km, recordings from crustal earthquakes worldwide are retained to constrain the magnitude scaling and geometric spreading. There is not a strong magnitude dependence of  $\delta B$ . For  $Z_{\text{tor}}$ , there is no trend in the residuals at high frequencies, in which the model increases the ground motion with increasing  $Z_{\text{tor}}$ . There is a potential difference in  $Z_{\text{tor}}$  scaling between regions at low to moderate frequencies, an effect that should be evaluated further in the future. The reverse style-of-faulting scaling is captured in the  $Z_{\text{tor}}$  scaling. This is confirmed by checking that the mean of event terms for reverse style-of-faulting earthquakes does not statistically differ from zero. For  $F_{\text{NM}}$ , there is also no strong bias in the residuals at high frequencies, but at the lower frequencies, potential regional differences exist. The normal faulting term is constrained by sparse data (10 events at 0.2 Hz, including six from Italy), so this term is not refined further. The dependence of the between-site residuals on  $V_{S30}$  is also evaluated. Overall, there is no apparent trend in  $\delta S2S$  versus  $V_{S30}$  or  $Z_1$ .

#### Within-Site Residuals

The dependence on the model parameters of the within-site residuals at  $f = 5.0$  Hz is given in Figure 5. The filled circles are individual residuals, and the filled diamonds with whiskers represent the mean and 95% confidence interval of the mean for binned ranges of the model parameter. Overall, there is no trend observed in  $\delta WS$  versus moment magnitude. The linear site response model is evaluated through the  $V_{S30}$  and  $Z_1$  dependence of the residuals. Overall, no strong trends are observed against  $V_{S30}$ , except for the highest  $V_{S30}$  values at low frequencies, in which the residuals are slightly positive, indicating model underprediction. The data are very sparse in this range (six records with  $V_{S30} > 1500$  m/s and 106 records with  $V_{S30} > 1200$  m/s). No strong  $Z_1$  dependencies on the within-site residuals are observed.

The distance scaling of the model is evaluated using the distance dependence of  $\delta WS$  as shown in Figure 5 ( $f = 5.0$  Hz). In addition, the distance dependence is evaluated using magnitude binned residuals, for example, Figure 6, in which the magnitude bin ranges are given in the figure legend. In the distance range of about 5–100 km, there are no strong trends or biases of the residuals. At low frequencies, for distances beyond 100 km, and in the  $M$  5.5–6.5 bin, the  $\delta WS$  residuals are biased positive. This is likely due to the relatively limited data within this bin. We believe that the model scaling is appropriate even though these particular residuals are not zero centered. Thus, neither the magnitude

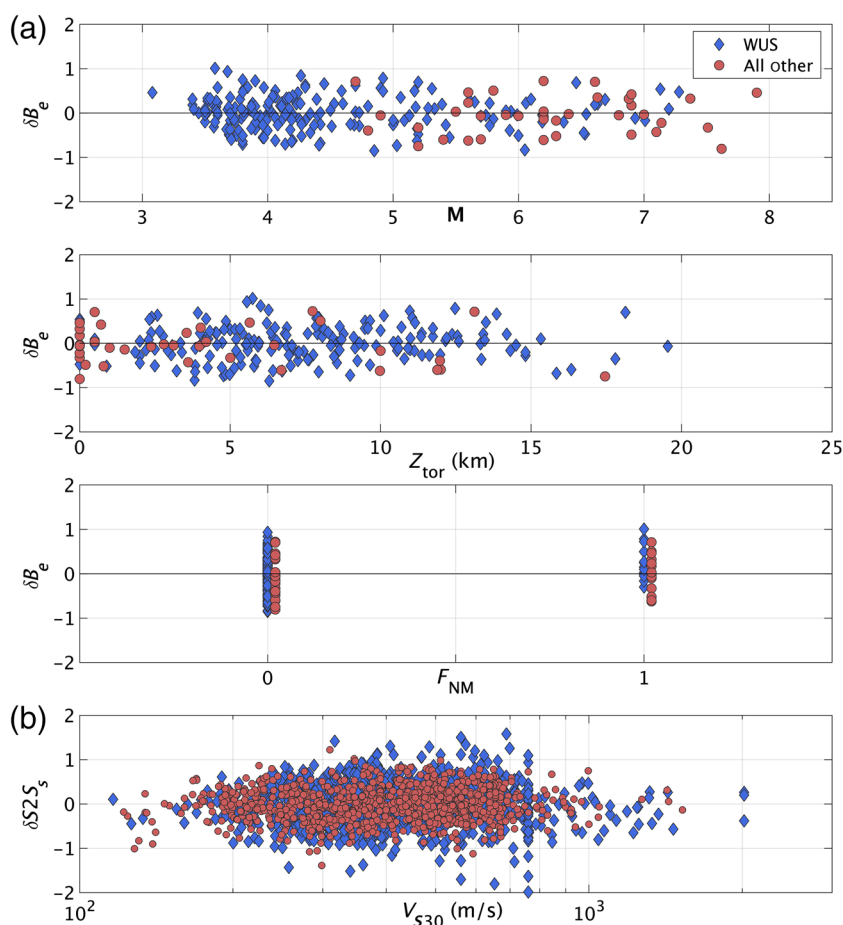


**Figure 4.** (a) Between-event residuals ( $\delta B_e$ ) versus  $M$ ,  $Z_{tor}$ , and  $F_{NM}$  and (b) between-site residuals ( $\delta S2S_s$ ) versus  $V_{S30}$ ,  $f = 5$  Hz. The color version of this figure is available only in the electronic edition.

nor distance scaling is adjusted to center these residuals. At distances shorter than 1 km and for frequencies greater than  $\sim 2$  Hz, there is a small systematic negative bias in the residuals (e.g., Fig. 5 indicating model overprediction). This means the near-fault saturation in this model is not as strong as implied by the data. The oversaturation of distance scaling (a peak in the distance scaling at distances larger than zero) is intentionally avoided in this model. Others, such as Graizer (2018), chose to incorporate oversaturation (with a peak in the distance scaling at about 5 km) into their GMMs. Because the available ground-motion data are sparse at such close distances, this model is compared with the saturation from finite-fault earthquake simulations to model the distance scaling (see the Model Summary section for more details). Based on these results and on the sparsity of the data, the small bias in the short-distance residuals is accepted.

## Model Summary

### Median Model

In this section, the median BA18 model behavior is summarized. In Figure 7, the median EAS from this model (solid

lines) are compared with spectra from the additive double-corner-frequency source spectral model (dashed lines) described by Boore *et al.* (2014). The double-corner-frequency spectra are computed using typical parameters for the WUS given by Boore (2003), including shear-wave velocity = 3.5 km/s, density = 2.72 g/cm<sup>3</sup>, stress-drop parameter  $\Delta\sigma = 50$  bars for  $M \geq 5$ ,  $\kappa = 0.027$  s, the Boore and Thompson (2015) finite-fault distance adjustment, the Boore and Thompson (2014) path duration for western North America, and the Boore (2016) crustal amplification model. We assume a magnitude dependence to the stress drop for  $M < 5$ . In Figure 7, we use  $\Delta\sigma = 25$  bars for  $M4$  and  $\Delta\sigma = 13$  bars for  $M3$ . The point-source spectral models are calculated using the software package SMSIM (Boore, 2005). The BA18 median model spectra are computed for a strike-slip scenario at  $R_{rup} = 30$  km, with  $Z_{tor} = 0$  km, and with the reference  $V_{S30}$  and  $Z_1$  conditions ( $V_{S30} = 1000$  m/s and  $Z_1 = 0.0089$  km).

Figure 7 shows overall good agreement between the median model and the additive double-corner-frequency source spectral model with typical WUS parameters, including a well-defined decrease in corner frequency with increasing  $M$ .

The theoretical corner frequency is related to the seismic moment by the equation:  $f_c = 4.906 \times 10^6 \times \beta_s \times (\Delta\sigma \times M_0)^{1/3}$  in which  $\beta_s$  is the shear-wave velocity in the vicinity of the site in kilometers per second and  $\Delta\sigma$  is the stress-drop parameter in bars (Boore *et al.*, 2014). The corner frequency is shown in Figure 7 (for  $\beta_s = 3.5$  km/s and  $\Delta\sigma = 50$  bars) with dashed vertical lines to help illustrate this relationship. At frequencies well below the corner frequency and for the far-field condition in which finite-fault effects are negligible, the spectra should be directly proportional to seismic moment ( $M_0$ ), and because  $M_0 = 10^{1.5M-16.05}$ , the spectra in this range should scale by  $10^{1.5} \approx 31.6$  for one magnitude unit. This approximate scaling at low frequencies is evident in Figure 7. An additional test for the low-frequency scaling  $M$  is in the Chiou and Youngs (2008) magnitude-scaling coefficient  $c_3$ , for which the theoretical value is  $\ln(10^{1.5}) \approx 3.45$ . At the lowest frequencies, coefficient  $c_3$  approximates this value (Fig. 2), so the EAS data are consistent with the theoretical value.

At frequencies between 10 and 30 Hz, there is a dip in the BA18 model spectra compared with the point-source spectra shown in Figure 7. This may be related to the region-specific attenuation parameters (geometric spreading and Q), in which the point source spectra use generalized models for

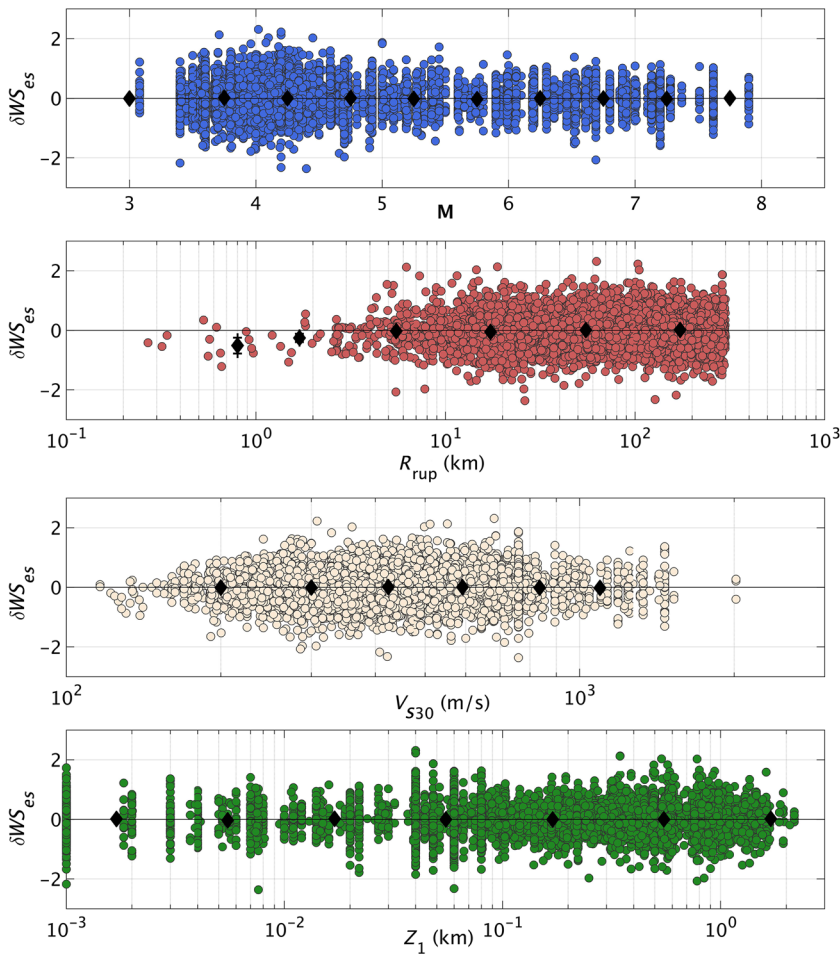


**Figure 5.** Within-site residuals ( $\delta WS_{es}$ ) versus  $M$ ,  $R_{rup}$ ,  $V_{S30}$ , and  $Z_1$  for  $f = 5$  Hz. The color version of this figure is available only in the electronic edition.

these attenuation parameters. The  $\kappa$ -based extrapolation in the BA18 model spectra begins at 24 Hz.

In Figure 8, the median EAS spectra from this model are shown for a set of scenarios. Figure 8a shows the spectra for a vertical strike-slip scenario with  $V_{S30} = 1000$  m/s at  $R_{rup} = 100$  km. Figure 8b shows the spectra for the same scenario but with  $V_{S30} = 500$  m/s at  $R_{rup} = 0$  km. In Figure 9, the distance scaling of the median model is shown for  $f = 0.2, 5,$  and  $20$  Hz. The distance scaling is compared with the Chiou and Youngs (2014) model for PSA (dashed lines) by scaling the PSA values to the  $R_{rup} = 0.1$  km EAS values. At 0.2 Hz, where the Q term coefficient ( $c_7$ ) is very small, the distance scaling is controlled by the geometric spreading terms, which includes a transition to  $R^{-0.5}$  scaling to model surface-wave geometric spreading at larger distances. At increasing frequencies, the effect of the Q term becomes more pronounced. In Figure 9c, the distance scaling is shown to deviate significantly from the Chiou and Youngs (2014) model, which has a magnitude dependence on Q. This difference can be explained by the differences between the EAS and PSA. At high frequencies, the PSA is strongly influenced by the predominant ground-motion frequency, as discussed

earlier. Because of this, the PSA scaling at 20 and 5 Hz is similar, but because the EAS at 20 Hz is directly representative of the ground motions in that frequency range, the EAS distance scaling is much stronger for 20 Hz than for 5 Hz.

The  $M$  scaling of the median EAS is shown in Figure 10 for a strike-slip surface rupturing scenario with reference  $V_{S30}$  and  $Z_1$  conditions, for  $f = 0.2$  and 5 Hz. The BA18  $M$  scaling is guided by broadband finite-fault simulations. The simulations were performed on the Southern California Earthquake Center (SCEC) Broadband Platform (Maechling *et al.*, 2015) v. 17.3 using simulation methods Graves and Pitarka (2015; hereafter, GP) and Atkinson and Assatourians (2014, also known as EXSIM). Both simulation methods were used to obtain broadband time histories for vertical strike-slip scenarios with  $M$  ranging from 6.5 to 8 and with stations arranged on constant  $R_{rup}$  bands. At each station, the EAS is calculated from the simulated acceleration time series for a range of frequencies, and the mean and standard deviation is calculated over all stations on each  $R_{rup}$  band. The results of these simulations, plotted as mean EAS versus  $M$  for a given frequency and rupture distance, are used to evaluate the near-source saturation of the  $M$  scaling and to compare with the scaling implied

by the data. Examples of these results are given in Bayless and Abrahamson (2018b; their figures 6.5–6.7). At very close distances, there is smaller high-frequency  $M$  scaling rate in EXSIM than in GP. Interestingly, this relationship is inverted at low frequencies. There is stronger  $M$  scaling rate in BA18 than there is in Chiou and Youngs (2014) (for PSA) at all frequencies. Based on these comparisons, we determine the EAS  $M$  scaling rate in this model is consistent with that from the simulations. The EAS should have some  $M$  scaling at zero distance even though the PSA is nearly fully saturated at high frequencies because the PSA is defined as the peak response of the oscillator over all time, meaning it is not affected by increased duration of the small amplitude part of the signal. Conversely, the EAS will continue to scale for large magnitudes at short distance because of the longer source durations.

Bayless and Abrahamson (2018b; their fig. 6.8) summarizes the linear portion of the site response scaling of BA18 with a set of example scenarios. Figure 11 illustrates the behavior of the nonlinear portion of the site response scaling. Figure 11a shows the scaling of the modified Hashash *et al.* (2018) nonlinear site term with  $M$ , for a scenario with  $R_{rup} = 30$  km and  $V_{S30} = 300$  m/s. Similarly, Figure 11b shows



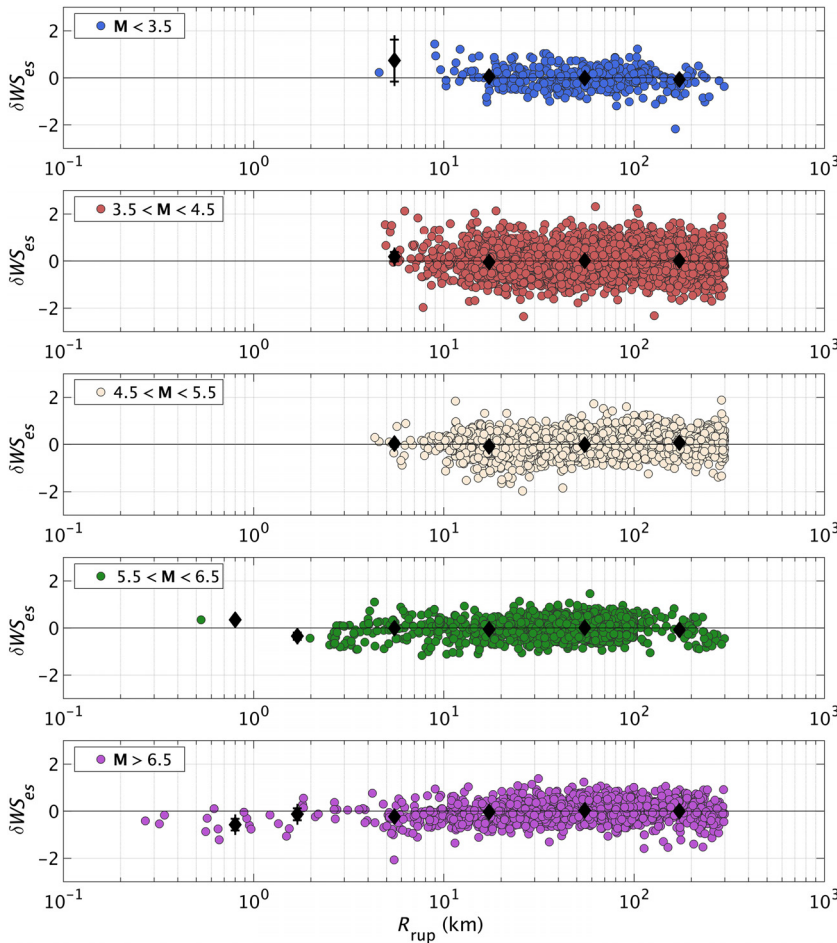


**Figure 6.** Within-site residuals ( $\delta WS_{es}$ ) versus  $R_{rup}$ , binned by  $M$  for  $f = 5$  Hz. The color version of this figure is available only in the electronic edition.

the scaling of the modified Hashash *et al.* (2018) nonlinear site term with  $R_{rup}$  for a scenario with  $M$  7 and  $V_{S30} = 300$  m/s.

### Standard Deviation Model

Prediction of the EAS (equation 6) requires a model for the aleatory variability. The random-effects method used leads to the separation of total residuals into between-event residuals ( $\delta B$ ) site-to-site residuals ( $\delta S_{2S}$ ) and single-station within-event residuals ( $\delta WS$ ), which have variance components  $\tau^2$ ,  $\phi_{S_{2S}}^2$ , and  $\phi_{ss}^2$ , respectively. The total standard deviation model (natural logarithm units) is given by

$$\sigma = \sqrt{\tau^2 + \phi_{S_{2S}}^2 + \phi_{ss}^2 + c_{1a}^2}, \quad (18)$$

in which  $c_{1a}$  is the difference between the regressed values of  $c_1$  and the constrained values of  $c_1$ , as described previously.

Figure 12 shows the standard deviations for each component of equation (18), as calculated directly from the regression analysis (all magnitudes). The increase observed in  $\tau$  at frequencies greater than  $\sim 3$  Hz is consistent with the behavior of response spectrum models (e.g., Abrahamson *et al.*, 2014;

Chiou and Youngs, 2014). This is believed to be the effect of  $\kappa$ , which is related to regional crustal damping, being mapped into the between-event terms. For a given earthquake, recordings in close proximity to the source will have similar  $\kappa$ , and the high frequencies of these recordings may be systematically above or below average. If there is a regional difference in kappa, then the regression treats this as an event-specific variation, which artificially increases  $\tau$ . Stafford (2017) also observed an increase in the variance components of the FAS with increasing frequency and hypothesized that the increase of  $\phi_{S_{2S}}$  reflects variations in  $\kappa$  across different sites.

The magnitude dependence of each aleatory term is modeled by equations (19a)–(19c). At low frequencies, the small-magnitude data have higher between-event standard deviation. This is also consistent with the Abrahamson *et al.* (2014) response spectrum model and could be related to the steeper magnitude scaling slope at low magnitudes and the uncertainty in small-magnitude source measurements (Abrahamson *et al.*, 2014). The standard deviations of the two within-event residuals do not have strong magnitude dependence at low frequencies. At higher frequencies,  $\tau$  does not show strong magnitude dependence, but  $\phi_{S_{2S}}$  and  $\phi_{ss}$

are larger for the small-magnitude data, which is again consistent with the Abrahamson *et al.* (2014) and Chiou and Youngs (2014) within-event variances. Higher within-event variability for small magnitudes may be related to the stronger effect of the high-frequency radiation pattern, which is reduced for larger magnitude events because of destructive interference from waves generated by different parts of the finite rupture (Abrahamson *et al.*, 2014).

$$\tau = \begin{cases} s_1 & \text{for } M < 4.0 \\ s_1 + \frac{s_2 - s_1}{2} (M - 4) & \text{for } 4.0 \leq M \leq 6.0, \\ s_2 & \text{for } M > 6.0 \end{cases}, \quad (19a)$$

$$\phi_{S_{2S}} = \begin{cases} s_3 & \text{for } M < 4.0 \\ s_3 + \frac{s_4 - s_3}{2} (M - 4) & \text{for } 4.0 \leq M \leq 6.0, \\ s_4 & \text{for } M > 5.5 \end{cases}, \quad (19b)$$

$$\phi_{ss} = \begin{cases} s_5 & \text{for } M < 4.0 \\ s_5 + \frac{s_6 - s_5}{2} (M - 4) & \text{for } 4.0 \leq M \leq 6.0. \\ s_6 & \text{for } M > 6.0 \end{cases}. \quad (19c)$$

At frequencies above  $\sim 20$  Hz, the model is constrained to smoothly transition to be flat in frequency space for all



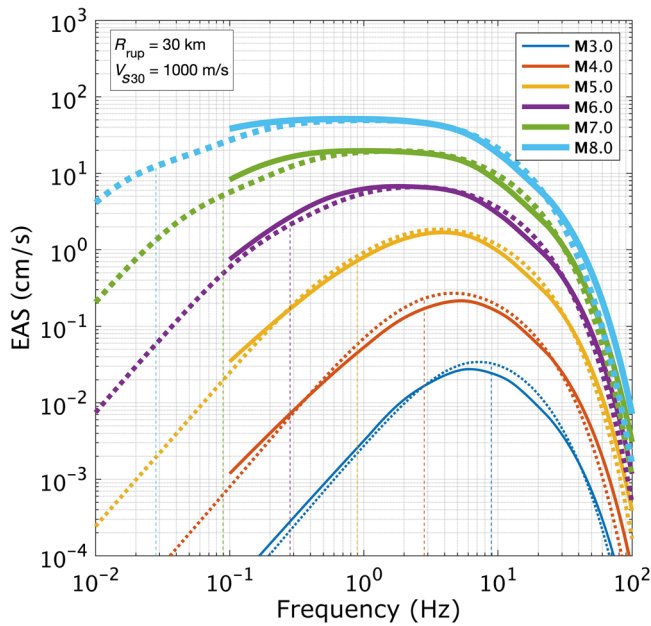


**Figure 7.** Median model spectra (solid lines) for a strike-slip scenario at  $R_{rup} = 30$  km, with  $Z_{tor} = 0$  km, and with the reference  $V_{S30}$  and  $Z_1$  conditions compared with the additive double-corner frequency source spectral model with typical western United States (WUS) parameters (dashed lines). To help visualize the decrease in corner frequency with increasing  $M$ , the theoretical corner frequency ( $f_c = 4.906 \times 10^6 \times \beta_s \times (\Delta\sigma \times M_0)^{1/3}$ ) for each magnitude is indicated by the vertical dashed lines. The color version of this figure is available only in the electronic edition.

components of  $\sigma$ . The frequency-dependent coefficients  $s_1$ – $s_6$  are given in the  $\text{\textcircled{E}}$  supplemental content to this article. The total standard deviation model for  $M$  3, 5, and 7 is shown in Figure 13. In Figure 14, the components of the standard deviation model are compared with those from Bora *et al.* (2019) and Stafford (2017). The strong differences observed between the three models can be attributed, in part, to the different datasets used by each group and to how the FAS GMM was developed. The Bora *et al.* (2019) model was developed using individual horizontal FAS components with high smoothing (Konno and Ohmachi, 1998 smoothing parameter equal to  $b = 40$ , equivalent to  $b_w = 0.157$ ) from a subset of the NGA-West2 data including multiple regions. The Stafford (2017) median FAS model was developed for unsmoothed FAS from a subset of the NGA-West1 database (Chiou *et al.*, 2008) using two methods: frequency-by-frequency regression and adapting a smooth point-source model to the data. The Stafford (2017) FAS standard deviation model makes use of the results using both methods.

The standard deviation model developed here is linear, meaning it does not account for the effects of nonlinear site response. As discussed by Al Atik and Abrahamson (2010) and Abrahamson *et al.* (2014), the nonlinear effects on the standard deviation are influenced by the variability of the rock motion, leading to a reduction in the soil motion variability at high frequencies. In Abrahamson *et al.* (2014), the standard deviation of the rock motion is estimated by removing the site

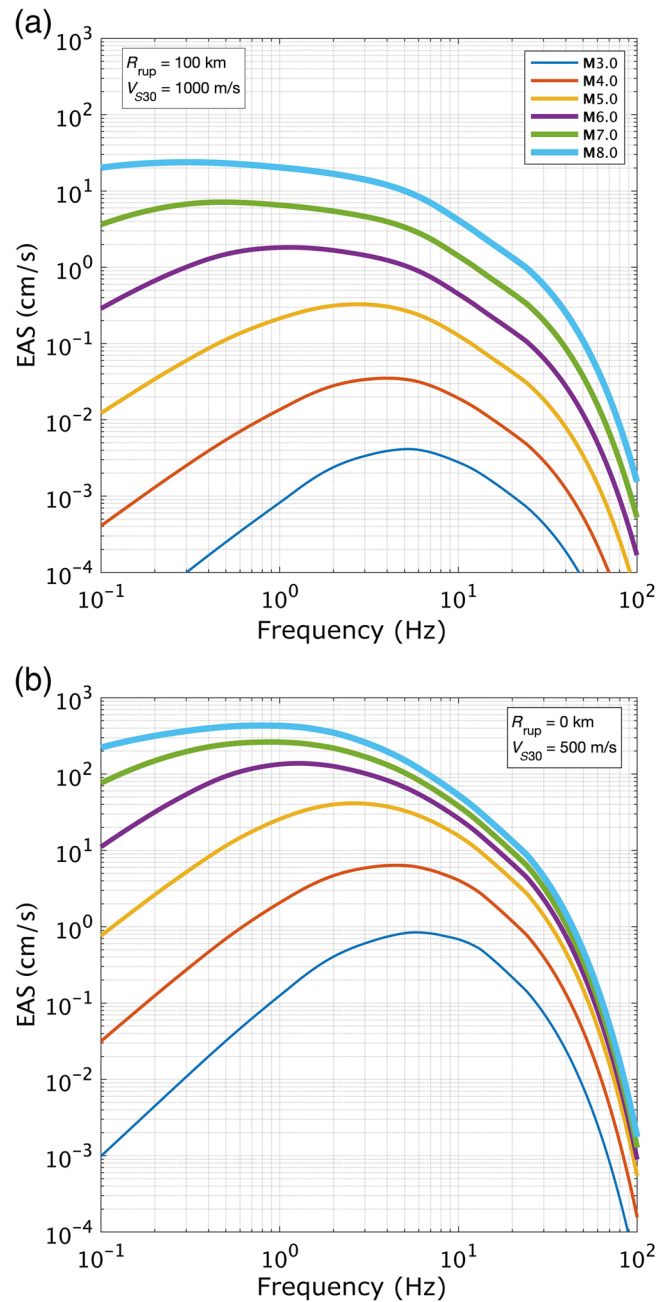


**Figure 8.** Median model EAS spectra for a set of scenarios: (a)  $V_{S30} = 1000$  m/s and  $R_{rup} = 100$  km and (b)  $V_{S30} = 500$  m/s and  $R_{rup} = 0$  km. The color version of this figure is available only in the electronic edition.

amplification variability (determined analytically) from the surface motion, and the variability of the soil motion is computed using propagation of errors. In a future update of the model, similar steps will be taken to account for the effects of nonlinear site response on the standard deviation.

#### Range of Applicability

The model is applicable for shallow crustal earthquakes in California. The model is developed using a database

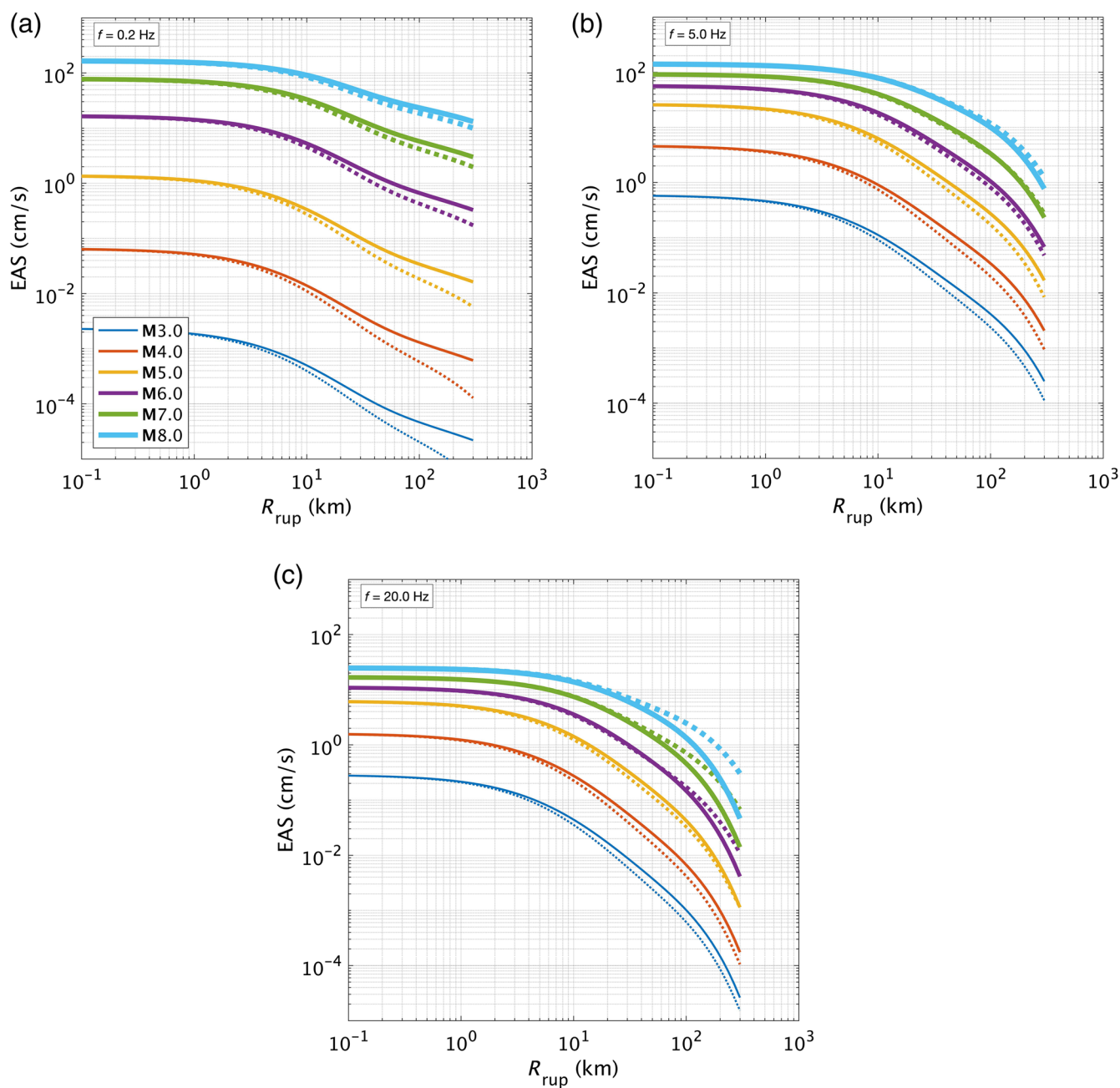


**Figure 9.** Distance scaling of the median EAS (solid lines) for a strike-slip scenario with reference  $V_{S30}$  and  $Z_1$  conditions, with increasing magnitude for (a)  $f = 0.2$ , (b)  $f = 5$ , and (c)  $f = 20$  Hz. For reference, the distance scaling of the Chiou and Youngs (2014) model for pseudospectral acceleration (PSA) is shown for the same scenarios with the dashed lines, in which the PSA values have been scaled to the  $R_{rup} = 0.1$  km EAS values. The color version of this figure is available only in the electronic edition.

dominated by California earthquakes but uses data worldwide to constrain the magnitude scaling and geometric spreading. The model is applicable for rupture distances of 0–300 km,  $M$  3.0–8.0, and over the frequency range 0.1–100 Hz. The  $V_{S30}$  range of applicability is 180–1500 m/s, although the model is not well constrained for  $V_{S30}$  values  $> 1000$  m/s. Models for the median and the aleatory variability of the EAS are developed. Regional models for Japan and Taiwan will be developed in a future update of the model. A

model for the interfrequency correlation of  $\epsilon_{EAS}$  is presented in Bayless and Abrahamson (2018c).

#### Limitations and Future Considerations

The model presented uses the ergodic assumption, as introduced by Anderson and Brune (1999). This means that the variability in the data from a broad geographic region (in this case, globally for the magnitude scaling and geometric

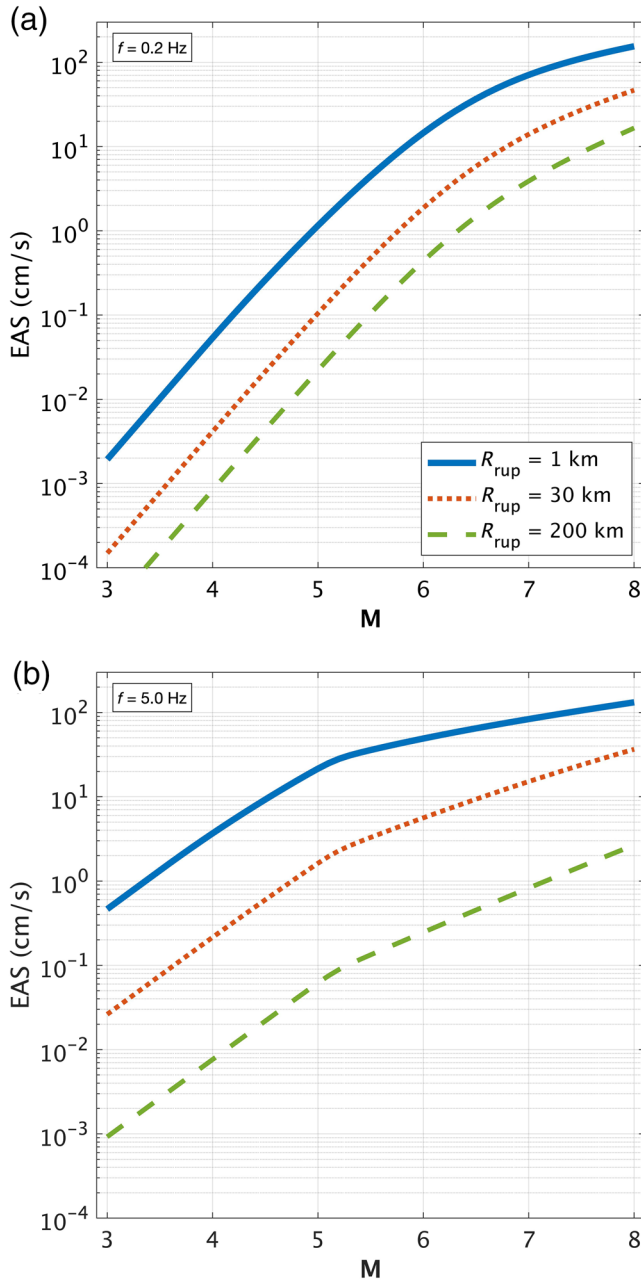


**Figure 10.**  $M$  scaling of the median EAS for a strike-slip surface rupturing scenario with reference  $V_{S30}$  and  $Z_1$  conditions, for (a)  $f = 0.2$  and (b)  $f = 5.0$  Hz. The color version of this figure is available only in the electronic edition.

spreading, and over California and western Nevada for the remaining parameters) are assumed to represent the variability of the ground motions over time for a given site in the target region. With this approach, the model is expected to be appropriate for general use in California but will be biased for a particular site. In an ergodic model, systematic site, path, and source effects are the dominant parts of the aleatory variability, making fully or partially nonergodic models attractive (Abrahamson, 2017). Developing a partially nonergodic model requires repeated observations of source, path,

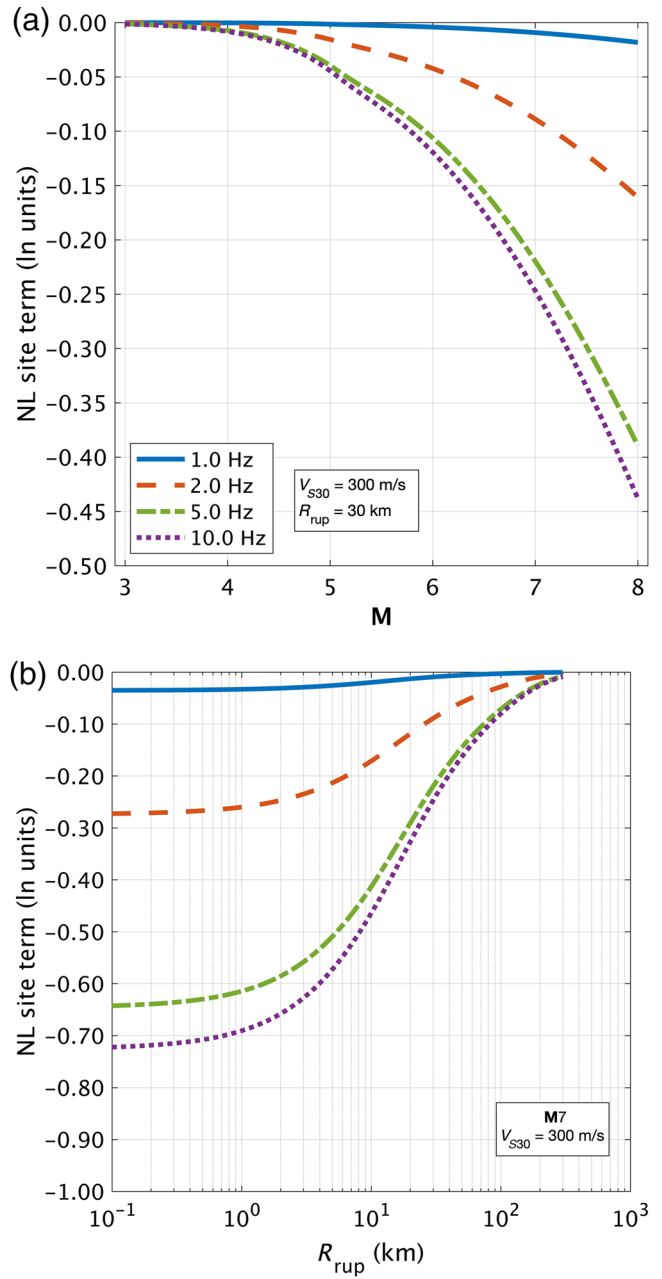


**Figure 11.** (a) Scaling of the modified Hashash *et al.* (2018) nonlinear site term with  $M$ , for  $R_{rup} = 30$  km and  $V_{S30} = 300$  m/s. (b) Scaling of the modified Hashash *et al.* (2018) nonlinear site term with  $R_{rup}$  for  $M$  7 and  $V_{S30} = 300$  m/s. The color version of this figure is available only in the electronic edition.

or site effects. For example, in this model, with multiple recordings at a site, the median site-specific amplification for the site is separated from the within-event residual. The cost of removing this systematic site term from the within-event aleatory variability leads to epistemic uncertainty in the site-specific site term (Walling, 2009). To develop a fully nonergodic model, all of the components of the total ground-motion variability that are caused by systematic effects for a given source and site must be removed (Abrahamson and Hollenback, 2012).



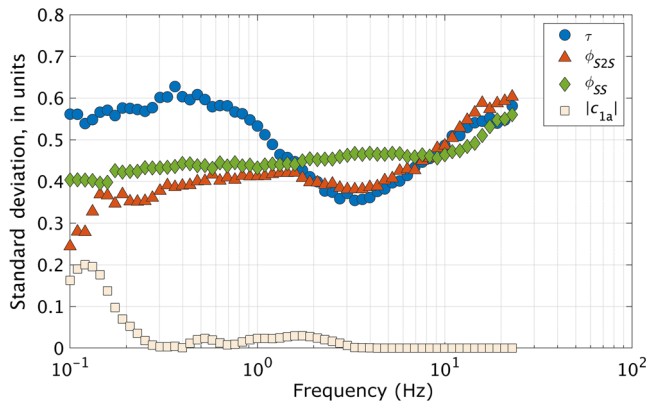


**Figure 12.** Standard deviation components calculated directly from the regression analysis for all magnitudes. The color version of this figure is available only in the electronic edition.

Incorporating regional differences into a GMM is a first step toward a partially nonergodic assumption (Kuehn and Scherbaum, 2016). To account for the known differences in regional crustal structure, regionalized models for Japan and Taiwan can be developed in a future model update. This will involve regionalizing the linear  $V_{S30}$  scaling ( $c_8$ ), soil depth scaling ( $c_{11}$ ), anelastic attenuation ( $c_7$ ), and spectral shape ( $c_1$ ) coefficients.

At frequencies  $>24$  Hz, this model uses a  $\kappa$ -based extrapolation. This approach required selecting a  $\kappa - V_{S30}$  relationship from the literature. Future improvements to the model may include explicit data regression at higher frequencies, developing a region-specific  $\kappa - V_{S30}$  relationship, or calculating one directly from the database used.

The effects of rupture directivity, hanging-wall scaling, and aftershock scaling are not explicitly included in the model. Therefore, these effects are accounted for in the total aleatory variability. The hanging-wall effect, characterized by increased ground-motion amplitudes on the hanging-wall side of dipping ruptures, is not well constrained by the data. For NGA-West2, Donahue and Abrahamson (2013) investigated these effects for response spectra using finite-fault simulations, and the results were incorporated in the Abrahamson *et al.* (2014) model. In a future update, a similar study for hanging-wall effects on the EAS could be incorporated into this model. The effects of rupture directivity on the EAS are also a potential future research topic. Finally, the effects of nonlinear site response on the standard deviation are not accounted for in this model, which can be addressed in a future update.

### Data and Resources

The ground-motion data were provided by the Pacific Earthquake Engineering Research Center (PEER) Next Generation Attenuation-West2 (NGA-West2) project (Ancheta *et al.*, 2014). Regression analyses and graphics production were performed using the numeric computing environment MATLAB ([www.mathworks.com](http://www.mathworks.com), last accessed

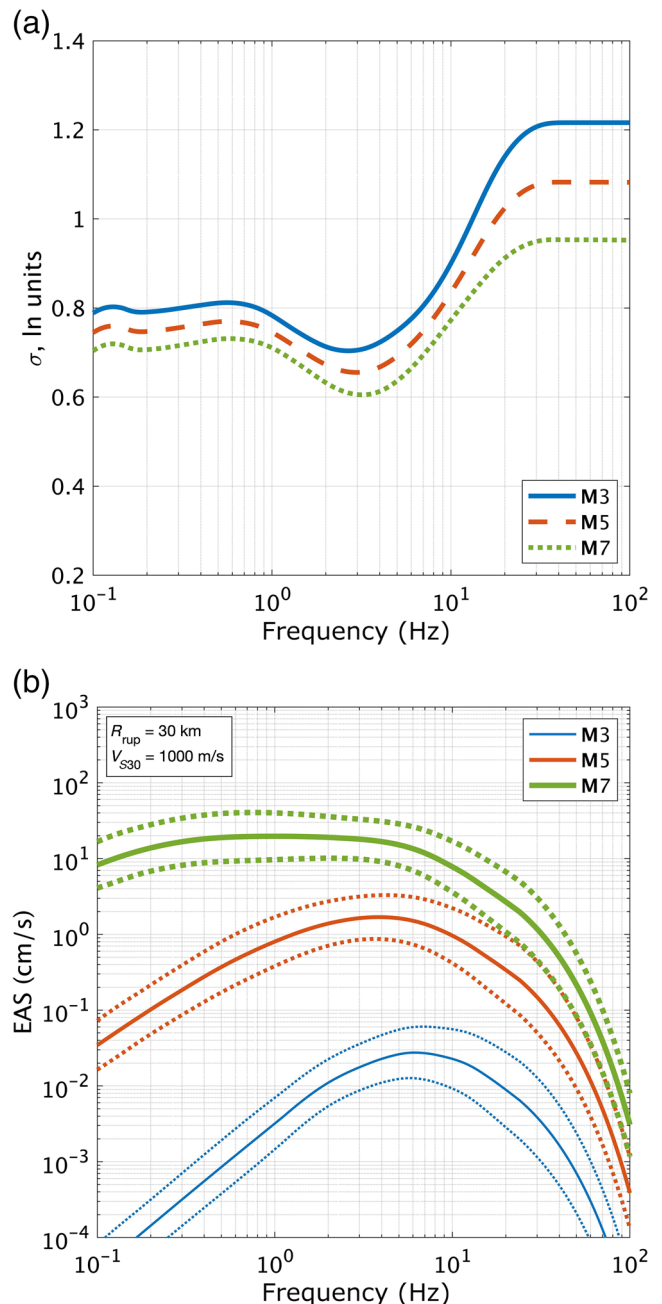


**Figure 13.** (a) Total standard deviation model for M3, 5, and 7. (b) Median (solid lines) and median plus and minus one  $\sigma$  (dashed lines) EAS spectra for M3, 5, and 7 scenarios. The color version of this figure is available only in the electronic edition.

March 2019). The finite-fault simulations were calculated on the Southern California Earthquake Center (SCEC) Broadband Platform (Maechling *et al.*, 2015). The point-source spectra were calculated using the SMSIM software provided by Dave Boore ([www.daveboore.com](http://www.daveboore.com), last accessed March 2019). The  $\text{\textcircled{E}}$  supplemental content to this article contains a zip file with a MATLAB program that implements the BA18 ground-motion model and a spreadsheet listing the model coefficients. The MATLAB function includes all model coefficients required to predict the median



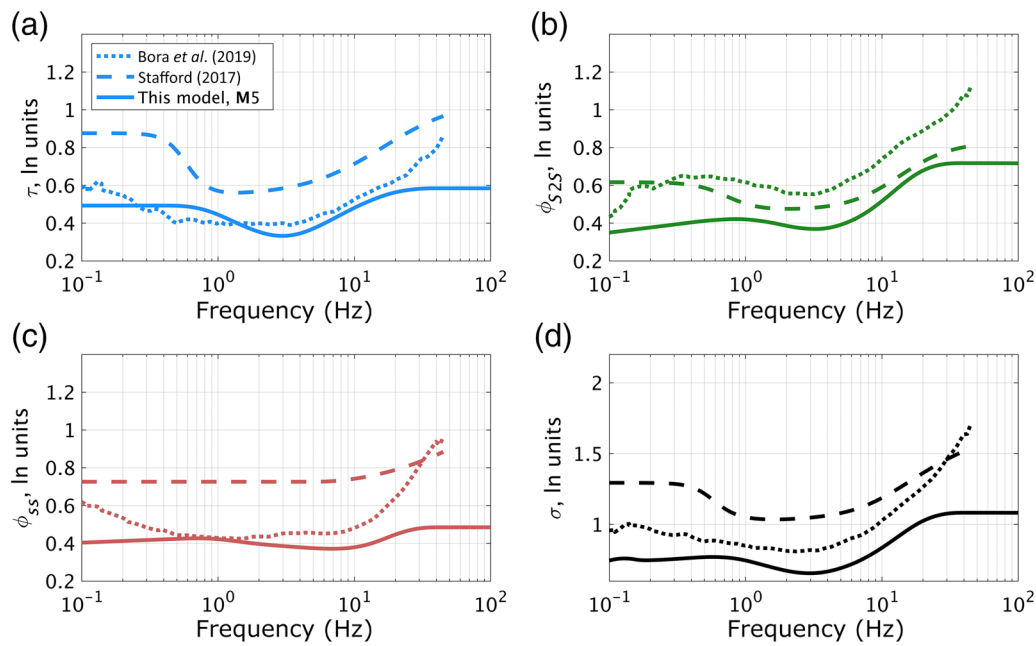


**Figure 14.** Comparison of the standard deviation components between the Bora *et al.* (2019), Stafford (2017) models, and this model, for an M 5 earthquake. (a–d) Comparison of  $\tau$ ,  $\phi_{S2S}$ ,  $\phi_{SS}$ , and  $\sigma$ , respectively. The color version of this figure is available only in the electronic edition.

effective amplitude spectrum and associated standard deviations over the frequency range 0.1–100 Hz.

### Acknowledgments

Thanks to Yousef Bozorgnia and Tadahiro Kishida at Pacific Earthquake Engineering Research Center (PEER) for providing the ground-motion database, to Ronnie Kamai for assistance with the regression software, to Albert Kottke for helpful discussions about the model residuals, to Youssef Hashash for sharing his site amplification model, and to two anonymous reviewers for their constructive comments and detailed feedback. This work was partially supported by the PG&E Geosciences Long-Term Seismic Program.

### References

- Abrahamson, N. A. (2006). Seismic hazard assessment: Problems with current practice and future developments, *Proc. of the First European Conference on Earthquake Engineering and Seismology*, Geneva, Switzerland, 17 pp.
- Abrahamson, N. A. (2017). Recent advances in seismic hazard, *Presentation given at the Pacific Rim Forum*, Berkeley, California, 23 January 2017.
- Abrahamson, N. A., and J. C. Hollenback (2012). Application of single-site sigma ground motion prediction equations in practice, *Proc. of the 15th World Conference on Earthquake Engineering*, 24–28 September 2012, Lisbon, Portugal, Paper No. 2536.
- Abrahamson, N. A., and W. J. Silva (1997). Empirical response spectral attenuation relations for shallow crustal earthquakes, *Seismol. Res. Lett.* **68**, no. 1, 94–127.
- Abrahamson, N. A., and R. R. Youngs (1992). A stable algorithm for regression analyses using the random effects model, *Bull. Seismol. Soc. Am.* **82**, 505–510.
- Abrahamson, N. A., W. J. Silva, and R. Kamai (2014). Summary of the ASK14 ground motion relation for active crustal regions, *Earthq. Spectra* **30**, 1025–1055.
- Aki, K. (1967). Scaling law of seismic spectrum, *J. Geophys. Res.* **72**, 1217–1231.
- Al Atik, L., and N. A. Abrahamson (2010). Nonlinear site response effects on the standard deviations of predicted ground motions, *Bull. Seismol. Soc. Am.* **100**, 1288–1292.
- Al Atik, L., N. A. Abrahamson, F. Cotton, F. Scherbaum, J. J. Bommer, and N. Kuehn (2010). The variability of ground-motion prediction models and its components, *Seismol. Res. Lett.* **81**, no. 5, 794–801.
- Ancheta, T. D., R. B. Darragh, J. P. Stewart, E. Seyhan, W. J. Silva, B. S.-J. Chiou, K. E. Wooddell, R. W. Graves, A. R. Kottke, D. M. Boore, *et al.* (2014). NGA-West2 database, *Earthq. Spectra* **30**, 989–1005.
- Anderson, J. G., and J. N. Brune (1999). Probabilistic seismic hazard assessment without the ergodic assumption, *Seismol. Res. Lett.* **70**, no. 1, 19–28.
- Anderson, J. G., and S. E. Hough (1984). A model for the shape of the Fourier amplitude spectrum of acceleration at high frequencies, *Bull. Seismol. Soc. Am.* **74**, 1969–1993.
- Atkinson, G. M., and K. Assaturians (2014). Implementation and validation of EXSIM (a stochastic finite-fault ground-motion simulation algorithm) on the SCEC broadband platform, *Seismol. Res. Lett.* **86**, no. 1, 48–60, doi: [10.1785/0220140097](https://doi.org/10.1785/0220140097).
- Bayless, J., and N. A. Abrahamson (2018a). Evaluation of the inter-period correlation of ground motion simulations, *Bull. Seismol. Soc. Am.* **108**, no. 6, 3413–3430, doi: [10.1785/0120180095](https://doi.org/10.1785/0120180095).
- Bayless, J., and N. A. Abrahamson (2018b). An empirical model for Fourier amplitude spectra using the NGA-West2 database, *PEER Rept. No. 2018/07*, Pacific Earthquake Engineering Research Center, University of California, Berkeley, California.
- Bayless, J., and N. A. Abrahamson (2018c). An empirical model for the inter-frequency correlation of epsilon for Fourier amplitude spectra, *Bull. Seismol. Soc. Am.* **109**, no. 3, 1058–1070, doi: [10.1785/0120180238](https://doi.org/10.1785/0120180238).
- Boore, D. M. (2003). Simulation of ground motion using the stochastic method, *P&A Geophys.* **160**, 635–675.
- Boore, D. M. (2005). SMSIM-Fortran programs for simulating ground motions from earthquakes: version 2.3—A revision of OFR 96-80-A, *U.S. Geol. Surv. Open-File Rept. 00-509*, revised 15 August 2005, 55 pp.
- Boore, D. M. (2016). Determining generic velocity and density models for crustal amplification calculations, with an update of the Boore and Joyner (1997) generic site amplification for VS(Z) = 760 m/s, *Bull. Seismol. Soc. Am.* **106**, 316–320.

- Boore, D. M., and E. M. Thompson (2014). Path durations for use in the stochastic-method simulation of ground motions, *Bull. Seismol. Soc. Am.* **104**, 2541–2552.
- Boore, D. M., and E. M. Thompson (2015). Revisions to some parameters used in stochastic-method simulations of ground motion, *Bull. Seismol. Soc. Am.* **105**, 1029–1041.
- Boore, D. M., C. Di Alessandro, and N. A. Abrahamson (2014). A generalization of the double-corner-frequency source spectral model and its use in the SCEC BBP validation exercise, *Bull. Seismol. Soc. Am.* **104**, 2387–2398.
- Bora, S. S., F. Cotton, and F. Scherbaum (2019). NGA-West2 empirical Fourier and duration models to generate adjustable response spectra, *Earthq. Spectra* **35**, no. 1, 61–93.
- Bora, S. S., F. Scherbaum, N. Kuehn, and P. J. Stafford (2016). On the relationship between Fourier and response spectra: Implications for the adjustment of empirical ground-motion prediction equations (GMPEs), *Bull. Seismol. Soc. Am.* **106**, no. 3, doi: [10.1785/0120150129](https://doi.org/10.1785/0120150129).
- Brune, J. N. (1970). Tectonic stress and spectra of seismic shear waves from earthquakes, *J. Geophys. Res.* **75**, 4997–5009.
- Chiou, B. S.-J., and R. R. Youngs (2008). An NGA model for the average horizontal component of peak ground motion and response spectra, *Earthq. Spectra* **24**, 173–216.
- Chiou, B. S.-J., and R. R. Youngs (2014). Update of the Chiou and Youngs NGA model for the average horizontal component of peak ground motion and response spectra, *Earthq. Spectra* **30**, 1117–1153.
- Chiou, B. S.-J., R. B. Darragh, N. Gregor, and W. J. Silva (2008). NGA project strong-motion database, *Earthq. Spectra* **24**, no. 1, 23–44.
- Donahue, J. L., and N. A. Abrahamson (2013). Hanging wall scaling using finite-fault simulations, *PEER Rept. 2013/14*, Pacific Earthquake Engineering Research Center, University of California, Berkeley, California.
- Douglas, J., and D. M. Boore (2011). High-frequency filtering of strong-motion records, *Bull. Earthq. Eng.* **9**, 395–409.
- Goulet, C. A., A. Kottke, D. M. Boore, Y. Bozorgnia, J. Hollenback, T. Kishida, A. Der Kiureghian, O. J. Ktenidou, N. M. Kuehn, E. M. Rathje, et al. (2018). Effective amplitude spectrum (EAS) as a metric for ground motion modeling using Fourier amplitudes, *2018 Seismology of the Americas Meeting*, Miami, Florida, 14–17 May 2018.
- Graizer, V. (2018). GK17 ground-motion prediction equation for horizontal PGA and 5% damped PSA from shallow crustal continental earthquakes, *Bull. Seismol. Soc. Am.* **108**, no. 1, 380–398, doi: [10.1785/0120170158](https://doi.org/10.1785/0120170158).
- Graves, R., and A. Pitarka (2015). Refinements to the Graves and Pitarka (2010) broadband ground-motion simulation method, *Seismol. Res. Lett.* **86**, 75–80, doi: [10.1785/0220140101](https://doi.org/10.1785/0220140101).
- Hanks, T. C. (1982). fmax, *Bull. Seismol. Soc. Am.* **72**, 1867–1879.
- Hashash, Y. M. A., J. Harmon, O. Ilhan, J. P. Stewart, E. M. Rathje, K. W. Campbell, W. J. Silva, and C. G. Goulet (2018). Modelling of site amplification via large scale nonlinear simulations with applications to North America, *Geotech. Earthq. Eng. Soil Dynam.*, Geotechnical Special Publication (GSP 291), Vol. 2018-June, no. 291, 523–537, doi: [10.1061/9780784481462.051](https://doi.org/10.1061/9780784481462.051).
- Hashash, Y. M. A., M. I. Musgrove, J. A. Harmon, D. R. Groholski, C. A. Phillips, and D. Park (2016). *DEEPSOIL V6.1, User Manual*, University of Illinois at Urbana-Champaign, Urbana, Illinois, 137 pp.
- Kamai, R., N. A. Abrahamson, and W. J. Silva (2014). Nonlinear horizontal site amplification for constraining the NGA-West2 GMPEs, *Earthq. Spectra* **30**, 1223–1240.
- Kim, B., Y. M. A. Hashash, J. P. Stewart, E. M. Rathje, J. A. Harmon, M. I. Musgrove, K. W. Campbell, and W. J. Silva (2016). Relative differences between nonlinear and equivalent-linear 1D site response analyses, *Earthq. Spectra* **32**, no. 3, 1845–1865.
- Kishida, T., O. Ktenidou, R. B. Darragh, and W. J. Silva (2016). Semi-automated procedure for windowing time series and computing Fourier amplitude spectra for the NGA-West2 database, *PEER Rept. No. 2016/02*, Pacific Earthquake Engineering Research Center, University of California, Berkeley, California.
- Konno, K., and T. Ohmachi (1998). Ground-motion characteristics estimated from spectral ratio between horizontal and vertical components of microtremor, *Bull. Seismol. Soc. Am.* **88**, 228–241.
- Kottke, A., E. Rathje, D. M. Boore, E. Thompson, J. Hollenback, N. Kuehn, C. A. Goulet, N. A. Abrahamson, Y. Bozorgnia, and A. Der Kiureghian (2018). Selection of random vibration procedures for the NGA east project, *PEER Rept. No. 2018/05*, Pacific Earthquake Engineering Research Center, University of California, Berkeley, California.
- Ktenidou, O., F. Cotton, N. A. Abrahamson, and J. G. Anderson (2014). Taxonomy of kappa: A review of definition and estimation approaches targeted to applications, *Seismol. Res. Lett.* **86**, no. 1, doi: [10.1785/0220130027](https://doi.org/10.1785/0220130027).
- Kuehn, N. M., and F. Scherbaum (2016). A partially non-ergodic ground-motion prediction equation for Europe and the Middle East, *Bull. Earthq. Eng.* **14**, 2629, doi: [10.1007/s10518-016-9911-x](https://doi.org/10.1007/s10518-016-9911-x).
- Maechling, P. J., F. Silva, S. Callaghan, and T. H. Jordan (2015). SCEC broadband platform: System architecture and software implementation, *Seismol. Res. Lett.* **86**, no. 1, doi: [10.1785/0220140125](https://doi.org/10.1785/0220140125).
- Pacific Earthquake Engineering Research Center (PEER) (2015). NGA-East: Median ground-motion models for the Central and Eastern North America region, *PEER Rept. No. 2014/05*, Pacific Earthquake Engineering Research Center, University of California, Berkeley, California.
- Stafford, P. J. (2017). Interfrequency correlations among Fourier spectral ordinates and implications for stochastic ground-motion simulation, *Bull. Seismol. Soc. Am.* **107**, no. 6, 2774–2791, doi: [10.1785/0120170081](https://doi.org/10.1785/0120170081).
- Villani, M. A., and N. Abrahamson (2015). Repeatable site and path effects on the ground-motion sigma based on empirical data from southern California and simulated waveforms from the cybershake platform, *Bull. Seismol. Soc. Am.* **105**, doi: [10.1785/0120140359](https://doi.org/10.1785/0120140359).
- Walling, M. A. (2009). Non-ergodic probabilistic seismic hazard analysis and spatial simulation of variation in ground motion, *Ph.D. Dissertation*, University of California, Berkeley, California.
- Walling, M., W. Silva, and N. Abrahamson (2008). Nonlinear site amplification factors for constraining the NGA models, *Earthq. Spectra* **24**, no. 1, 243–255.

**Jeff Bayless**

AECOM  
 One California Plaza, 300 S Grand Avenue  
 Los Angeles, California 90071 U.S.A.  
[jeff.bayless@aecom.com](mailto:jeff.bayless@aecom.com)

**Norman A. Abrahamson**

Department of Civil and Environmental Engineering  
 University of California  
 3021 Ghausi Hall, One Shields Avenue  
 Davis, California 95616 U.S.A.

Manuscript received 27 March 2019;  
 Published Online 10 September 2019